HIGH-MASS PROTO-STELLAR CANDIDATES - II: DENSITY STRUCTURE FROM DUST CONTINUUM AND CS EMISSION

H. Beuther, P. Schilke, K.M. Menten beuther@mpifr-bonn.mpg.de, schilke@mpifr-bonn.mpg.de, kmenten@mpifr-bonn.mpg.de Max-Planck-Institut für Radioastronomie, Auf dem Hügel 69, 53121, Germany

F. Motte motte@submm.caltech.edu

California Institute of Technology, MS 320-47, Pasadena, CA 91125, USA

 $\begin{array}{c} T.K. Sridharan\\ tksridha@cfa. harvard. edu \end{array}$

Harvard-Smithsonian Center for Astrophysics, 60 Garden Street, MS 78, Cambridge, MA 02138, USA.

F. WYROWSKI wyrowski@astro.umd.edu
Department of Astronomy, University of Maryland, College Park, USA

Version from October 22, 2018

ABSTRACT

We present a detailed 1.2 mm continuum and CS spectral line study of a large sample of 69 massive star forming regions in very early stages of evolution, most of them prior to building up an ultracompact HII region. The continuum data show a zoo of different morphologies and give detailed information on the spatial distributions, the masses, column densities and average densities of the whole sample.

Fitting the radial intensity profiles shows that three parameters are needed to describe the spatial distribution of the sources: constant emission from the center out to a few arcsec radius followed by a first power law intensity distribution which steepens further outside into a second power law distribution. The inner flat region is possibly caused by fragmentation of the large scale cores into smaller sub-sources, whereas the steeper outer power law distributions indicate finite sizes of the cores.

Separating the sources into sub-samples suggests that in the earliest stages prior to the onset of massive star formation the intensity radial distributions are rather flat resembling the structure of intensity peaks in more quiescent molecular clouds. Then in the subsequent collapse and accretion phase the intensity distributions become centrally peaked with steep power law indices. In this evolutionary stage the sources show also the broadest C³⁴S linewidth. During the following phase, when ultracompact HII regions evolve, the intensity power law radial distributions flatten out again. This is probably caused by the ignited massive stars in the center which disrupt the surrounding cores.

The mean inner power law intensity index m_i $(I \sim r^{-m_i})$ is 1.2 corresponding to density indices p $(n \sim r^{-p})$ of 1.6. In total the density distribution of our massive star formations sites seem to be not too different from their low-mass counterparts, but we show that setting tight constrains on the density indices is very difficult and subject to many possible errors.

The local densities we derive from CS calculations are higher (up to one order of magnitude) than the mean densities we find via the mm-continuum. Such inhomogeneous density distribution reflects most likely the ubiquitous phenomenon of clumping and fragmentation in molecular clouds. Linewidth-mass relations show a departure from virial equilibrium in the stages of strongly collapsing cores.

Subject headings: stars:formation - stars: massive - ISM: hot cores

1. INTRODUCTION

In recent years much more attention is being paid to high-mass star formation. Massive stars release huge amounts of energy in the interstellar medium, from massive bipolar outflows at their birth to strong UV radiation throughout their lifetime and terminating supernovae at their very end, and are thus shaping the interstellar medium in galaxies. In the past, limited spatial resolution and low sensitivity made investigations of those regions difficult to impossible. However, technological advances in the last decade, e.g., the advent of mm-interferometers and bolometer-arrays in the mm- and sub-mm range made it feasible to study even the youngest stages of high-mass star formation – prior to ultracompact HII regions – in much more detail than it was possible before (e.g. Cesa-

roni et al. 1994; Molinari et al. 1998; Sridharan et al. 2001). The earliest stages of High-Mass Proto-stellar Objects (HMPOs) are characterized observationally by high luminosities, strong dust emission and very weak or no detectable free-free emission at cm-wavelengths.

Global properties of the sample under study here were presented by Sridharan et al. (2001). We are now focusing on a detailed analysis of the density, mass and column density structure of the dust cores of this sample of HMPOs. Mapping at 1.2 mm with the IRAM 30 m telescope reveals the distribution of all dust – warm and cold – with high enough spatial resolution (11" correspond to 0.1-0.25 pc at typical distances between 2 & 5 kpc) to resolve the cores into substructures. The dust emission at this wavelength is optically thin, and the data allow determination of the gas and dust column densities, visual extinction, masses

and average densities. These parameters are important ingredients in the characterization of massive star formation sites.

Since the sources are resolved the dust maps offer the opportunity of a structure analysis of the HMPOs, and we present and discuss the radial intensity distributions of our whole sample. Comparisons of radial intensity and density profiles with observations of low-mass star formation sites and with predictions of different star formation theories (e.g. isothermal or logatropic equations of state, Shu et al. (1987); McLaughlin & Pudritz (1996)) are essential to understand similarities and differences between low-mass and high-mass star formation and collapse processes.

(Motte & André 2001) studied isolated and clustered proto-stellar envelopes, and they found that isolated protostellar envelopes exhibit density profiles like $n \sim r^{-2}$ as predicted by the standard model of star formation by Shu (1987). In contrast to that, proto-stellar envelopes in clusters are found to be induced in compact condensations resembling more finite-sized Bonnor-Ebert spheres than singular isothermal pheres, which suggests that dynamical proto-stellar models are more appropriate (Motte & André 2001; Whitworth & Summers 1985). Recent mid-infrared absorption studies of low-mass prestellar cores revealed a flattening of the very inner parts of the radial profiles as well as a steepening of them further outside (Bacmann et al. 2000). The high-mass regime is less well observed, but recent studies of ultracompact HII regions and/or hot cores indicate that their overall density profiles are somewhat shallower like $n \sim r^{\alpha}$ with $-1.0 < \alpha < -1.5$ than their low-mass counterparts, as predicted by e.g. logatropic equations of state (v.d. Tak et al. 2000; Hatchell et al. 2000). A physical interpretation of this is that in low-mass objects thermal support is the main resisting force against gravitational collapse, while for massive objects non-thermal support is necessary (Myers & Fuller 1992; McLaughlin & Pudritz 1996). It also has to be mentioned that earlier studies of ultracompact HII regions found density distribution of the molecular gas more like r^{-2} (Garay & Rodriguez 1990; Heaton et al. 1993). Those discrepancies are not finally solved.

We also observed a large fraction of the sample with the 30-m telescope in various lines of CS and and its isotopomer C³⁴S. Using a LVG code we derive local gas densities and CS column densities and discuss deviations from the average densities derived from dust emission. Additionally, the line width information is used as an evolutionary indicator in correlation with the radial indices. Further correlations between different parameters based on dust and CS emission are discussed.

2. Observations

2.1. Millimeter continuum

The MPIfR 37 element bolometer array MAMBO (Kreysa et al. 1998) at the IRAM 30-m telescope was used to image the 1.2 mm dust continuum emission of the whole sample. This survey was done in three sessions between February 1998 and February 2000. The passband of these bolometers has an equivalent width of approximately 80 GHz and is centered at $\nu_{\rm eff} \sim 240$ GHz.

The images were observed in the dual-beam on-the-fly

mapping mode. The telescope is scanned continuously in azimuth along each row while the secondary is wobbling in azimuth with a wobbler throw of 50". We used a scanning velocity of 6"/sec with a sampling frequency of 2 Hz. Each Scan was separated by 5" in elevation. Typical map sizes with the 37 element array are $300'' \times 240''$. Due to being strong sources, most of the maps were obtained as back-up projects during rather poor weather conditions (average zenith opacity ~ 0.3). The average rms in the final maps is 10-15 mJy/beam. The overall calibration uncertainty is estimated to approximately 20%.

Data reduction was done mainly with the MOPSI software package (Zylka 1998) and for a few sources with NIC (Broguière et al. 1995). Baselines were fitted in time and space. Correlated noise (skynoise) was subtracted in a radius of 23", the flat field for correlated noise was calculated within the sky noise routine by Zylka & Haslam (in prep.).

2.2. CS observations

We observed the J=2-1,3-2,5-4 lines of CS and $C^{34}S$ in three nights between the 31. October and the 3. November 2000 with the IRAM 30-m telescope in a large fraction of sources from our sample remotely from the MPIfR in Bonn/Germany. The center positions were the mm-continuum peak positions, and we observed 9 point maps with a 6'' spacing to map out the beam of the 2–1 line with the 5–4 and 3–2 lines. Calibration errors are estimated to be around 30%. Additional observing parameters are presented in Table 1.

3. Results

3.1. Dust morphologies

Massive dust cores were detected in all sources of our sample. Figure shows all images (absolute IRAS coordinates are given in Sridharan et al. 2001), while Table 2 presents the observational parameters, i.e. the number of identified cores per source (the numbers in the Table correspond to the labeled numbers in Figure), derived peak and integrated fluxes, position offsets, sizes of the major and minor axis of the sub-sources and the positional angle (PA), the latter were derived by 2d Gaussian fits to all sources. The sub-sources were identified by eye because other more systematic identification criteria (such as 10% contours or 10σ levels) failed in identifying all sources. Integrated fluxes were determined by sensibly chosen polygons around the identified sources (and are estimated to be accurate at a 20% level). In the case of isolated sources the polygons correspond to the 5% levels of the peak emission, whereas for clustered sources, we had to separate the sub-cores by eye.

We found 154 separate sub-sources in the 69 images, i.e. an average of 2.2 sub-sources per field. This number is higher than found in other samples of massive star formation sites, e.g. 1.1 (v.d. Tak et al. 2000), 1.8 (Hatchell et al. 2000) or 1.3 (Hunter et al. 2000). This is mainly due to the larger observed fields in our survey ($\approx 16 \text{ arcmin}^2$ in contrast to $4-9 \text{ arcmin}^2$ in the other samples), the number of sources per arcmin² does not vary strongly throughout the different samples. Most likely the majority of the single-dish cores split up into a number of sub-cores again

at even higher resolution because of the clustered mode of massive star formation.

Morphologically the sources resemble a zoo of different features: while many are centrally peaked, massive cores (e.g. 05553+1631, 18264-1162) with maybe smaller sub-sources nearby (e.g.18182-1433, 19266+1745) others show multiple associated, massive cores (e.g. 1208, 18310-0825), elongated structures (e.g. 1800, 20081+2720), larger filaments (e.g. 18223-1243, 19175+1357) and a few with less peaked features (e.g. 18540+0220, 19282+1814). We refrain from a systematic morphological classification, because many features are subject to resolution and projection effects, and a formal classification would be misleading. Nevertheless, the diversity of sources offers the chance to study many different aspects of massive star formation at its earliest evolutionary stages and its evolution in time: are the less peaked sources younger than the peaked ones, is the density structure different from the low mass case and if so, what does that imply, how do different sources interact with each other?

As can be seen from Table 2, the large majority of sources is resolved by the 11" beam. However, higher resolution interferometric observations of a few sources (Beuther et al., in prep.) reveal that the cores contain sub-structures which are not resolved by the single-dish observations. Combining both observations indicate that central, small condensations exist, which are embedded in larger cores observed at lower angular resolutions.

Other features of the dust cores – molecular line emission, maser emission, weak cm emission – are discussed in §4.1.1 and Sridharan et al. (2001).

3.2. Column densities, visual extinction, masses and average densities

The 1.2 mm continuum is mainly due to emission from optically thin dust (Hildebrand 1983). Following the approach outlined in Hildebrand (1983) we calculate the beam-averaged gas column density and the mass of the cores to

$$\begin{split} M_{\rm gas} &= \frac{1.3 \times 10^{-3}}{J_{\nu}(T_{\rm dust})} \frac{a}{0.1 \mu \rm m} \frac{\rho}{3 \rm g cm^{-3}} \frac{R}{100} \frac{F_{\nu}}{\rm Jy} \\ &\times \left(\frac{D}{\rm kpc}\right)^2 \left(\frac{\nu}{2.4 \rm THz}\right)^{-3-\beta} \ [{\rm M}_{\odot}] \\ N_{\rm gas} &= \frac{7.8 \times 10^{10}}{J_{\nu}(T_{\rm dust})\Omega} \frac{a}{0.1 \mu \rm m} \frac{\rho}{3 \rm g cm^{-3}} \frac{R}{100} \frac{F_{\nu}}{\rm Jy} \\ &\times \left(\frac{\nu}{2.4 \rm THz}\right)^{-3-\beta} \ [{\rm cm}^{-2}] \end{split}$$

where $J_{\nu}(T_{\rm dust}) = [\exp(h\nu/kT_{\rm dust}) - 1]^{-1}$ and Ω, a, ρ, R and β are the beam solid angle, grain size, grain mass density, gas-to-dust ratio and grain emissivity index for which we used the values $0.1\mu m$, 3g cm⁻³, 100 and 2, respectively (Hunter 1997; Hunter et al. 2000). The dust temperatures $T_{\rm dust}$ (ranging between 30 K and 60 K) are obtained by greybody fits to the IRAS- and mm-data (Sridharan et al. 2001). Systematic errors in these quantities are prevalent for the mass determination, e.g. the grain emissivity index β is reported to vary at least between 1.75 and 2.5 between the Orion photon-dominated

region and the Orion ridge (Lis et al. 1998), but work on massive star formation regions (Hunter 1997; Molinari et al. 2000) supports the use of a value of 2 on the average for such objects. Higher dust opacity indices as proposed by Ossenkopf & Henning (1994) would result in masses and column densities about a factor 4 lower, whereas lower temperatures – as proposed by NH₃ observations (Sridharan et al. 2001) – would increase the derived parameters more than a factor of two. The approach outlined above is used by us because recent observations of ultracompact HII regions (Hunter 1997; Hunter et al. 2000) were analyzed similarly, and a consistent data analysis is essential when comparing different observations. Taking into account all the possible errors and uncertainties we estimate the mass and column density to be correct within a factor of 5. Additionally, we calculated the visual extinction $A_v = N_{\rm gas}/0.94 \times 10^{21}$ (Frerking 1982) and the average density n_{gas} by dividing the column density by the average of the major and minor source size at the given distances (Sridharan et al. 2001). All the derived quantities are presented in Table 3. A comparison of the masses and luminosities of this sample with ultracompact HII regions is presented in Sridharan et al. (2001).

Beam averaged column densities of the main clumps range around a few times 10^{23} cm⁻², which correspond to a few 100 magnitudes of visual extinction. There are three exceptions (18089-1732, 18182-1433 and 18264-1152) with extremely high column densities as large as 10^{24} cm⁻² corresponding to a visual extinction of 10^4 . These sources are prominent from our other observations as well (Sridharan et al. 2001): they show no cm-emission down to 1 mJy, have water and methanol maser emission and are strong in all molecular lines we observed so far, outflow tracers as well as dense gas tracers. Many of the secondary clumps have column densities below 10^{23} cm⁻², which might correspond to lower mass star formation sites associated and interacting with the main massive cores.

While the column density and correspondingly the visual extinction are distance independent quantities the derived densities and masses suffer from ambiguities basing on the kinematic distance determination (Sridharan et al. 2001). Therefore Table 3 gives always a far and a near value for masses and densities (if just a far value is listed, we could resolve the distance ambiguity). The masses of the main cores are very high ranging from hundreds to a few thousand M_{\odot} , and for the far distance masses of $10^4~{\rm M}_{\odot}$ are reached. The most massive cores correspond to the sources with the highest column densities. The masses of the adjacent sub-cores were calculated using the same T_{dust} as for the main cores, but it is possible that those sub-cores are colder, which makes us underestimating the masses and column densities. Future independent temperature determinations of each sub-core are of great interest.

Additionally, we derived the average densities of the cores, and again we see differences between the main cores and the secondary cores. Average densities of the main components are mostly a few times 10⁵ cm⁻³, while the less massive secondary clumps are about one order of magnitude less dense.

3.3.1. Observational limitations of the intensity distributions

The maps are a two-dimensional intensity distribution, which is a convolution of the intrinsic intensity distribution with the telescope beam and which is also affected by the mapping technique. The intrinsic intensity distribution is a function of the density and temperature fields of the source, quantities which we ultimately want to derive. To interpret our results we have to consider carefully how all these factors affect the observations.

The intensity distribution of a source is convolved with the beam of the telescope, which limits the smallest observable spatial scale down to the HPBW. But theoretical work (Adams 1991) as well as simulations (Motte & André 2001) show that the convolution of the intensity distribution with the beam does not affect scales larger than the beam significantly.

However, effects of the dual-beam mapping technique (Emerson et al. 1979) and the size of the array have to be taken into account when analyzing larger scale source structures. Motte & André (2001) showed that part of the emission is filtered out due to the dual-beam mapping technique if there is a gradient of emission at the edge of the map. For most of our maps the emission decreases below the noise already far away from the edge of the map, which causes an ambiguity in the sense that we do not know whether the sources extend outside the maps below our sensitivity limit or whether the sources are fully contained in our mapped area and maybe just embedded in a constant low level plateau of the surrounding cloud. In the latter case of a constant plateau no spatial filtering effects the data. But as spatial filtering due to low level emission of the sources might steepen the radial profiles slightly, we simulated observations (similarly to those simulations outlined in Motte & André 2001) for our map sizes and found that the possible steepening due to spatial filtering is largely compensated by flattening effects caused by the error beam lobe of the 30m telescope. In any case, the power law index of the radial intensity profile measured over radii smaller than 50" only needs to be corrected by values < 0.2. Regions outside this radii still give information about morphology, number of sub-sources etc., but the absolute profiles there have to be taken more cautiously.

Hence in our analysis we concentrate on the range of radii between 11" and 50" from the center since that should reflect the intrinsic radial profiles reasonably well. Structure on scales smaller than the HPBW of 11" cannot be resolved, but the data constrain the integrated flux.

3.3.2. Radial intensity profiles and fitting results

As already mentioned in the Introduction, different star formation theories predict different density distributions of the core envelopes: e.g. singular isothermal spheroids result in proto-stellar density power law distributions $n \sim r^{-2}$ (Shu et al. 1987; Whitworth & Summers 1985), whereas logatropic equations of state predict flatter distributions $n \sim r^{-\alpha}$, with 1.0 (McLaughlin & Pudritz 1996). Therefore, to probe theories we try to fit our data by power law distributions.

Although the observed maps show substructure and multiple sources are a common phenomenon, most of the

clumps themselves are spherical to first order. But noncircular deviations most likely correspond to substructures in the core center than to changes in power law distributions, because comparing power law distribution s for cuts at various position angles generally produces similar power law indices. Therefore we produce the radial profiles by averaging the observed intensities in circular annuli of 4''(slightly less than Nyquist sampling) around the peak position. If adjacent and secondary sources distort the circular averaging significantly those ranges are not considered for fitting profiles. Fitting the data between 12'' and 52''by one power law gives poor results. Introducing a break at 32" (half of the fittable range) and fitting the data by two power laws reveals that in most cases the two power law fits are better, i.e. they have a far lower χ^2/ν (sum of squared deviations between fit and data divided by the degrees of freedom) than the single power law fits.

This basically says that power laws are not a very good description of the structure, but for simplicity's sake and for comparison with theoretical models, we still fit the data in these terms. We are aware that the break at 32" is arbitrary, because of the different distances and linear sizes of the sources, but we choose this approach for practical reasons. Introducing another varying break parameter would increase the degrees of freedom further, which is not desirable with altogether only 10 useable spatial positions. The exact location of the outer break is not crucial to the result that a single power law fit is inadequate. We also stress that while the exact values of the power law indeces do depend on the particular location of the outer break, our qualitative result, the steepening outwards, is not affected by the exact location. Combining all intrinsic errors (noise, steepening of the profiles by spatial filtering, flattening of the profiles due to the error beam, calibration, fitting error etc.) we estimate the σ_m of the radial profiles $I \sim r^{-m}$ to $\Delta m \sim 0.3$ (see also Motte & André 2001). The inner and outer profiles (all inside the radii of $\sim 60''$) are affected very similarly by the observational problems outlined in $\S 3.3.1$.

Our fitting procedure uses 3 parameters: the outer region from 32'' to 52'' is fitted by one power law $I \propto r^{-m_o}$ followed by a power law $I \propto r^{-m_i}$ out to 32''. Since the flux is finite, this power law has to stop somewhere, and we model the central region with constant intensity inside a breakpoint b. Those models were convolved with the beam of 11'' and b and m_i were fitted simultaneously to the data, whereas m_o was fitted directly to the data, because at those scales the effect of the beam is negligible.

The results are presented in Table 3 and a few example fits are shown in Fig. Figure (a) presents the distribution of inner radial indices m_i with a mean of 1.2 and a broad peak around 1.4. Fewer outer fits were possible due to secondary sources or too weak emission in that regions. An even better determination of the outer power law indices requires observing maps of a far larger extent, but the steepening in the outer region is a significant feature in a large fraction of sources. Approximately 65% of the sources, where m_o was determinable, show a steepening $m_o - m_i \geq 0.4$ ($\sigma_m \sim 0.3$) with an average $m_o - m_i \sim 0.6$ (see Fig. (c)). While the 1σ error of an individual determination is 0.3, the large number of sources make the qualitative result of a significant steepening outwards re-

liable. We also want to point out that in only one case (18553+0414) we find a flattening towards the outer core. In the case of low-mass sources a steepening in the outer region has recently been shown by Bacmann et al. (2000) and Alves et al. (2001) with the totally different techniques of mid-infrared and near-infrared absorption studies, respectively, which both do not have spatial filtering effects.

3.4. CS and $C^{84}S$ observations

We observed CS and $C^{34}S$ in 89 clumps (54 sources) and detected the CS(2-1) and (3-2) line in all of them. This is not a surprise because one of the original sample criteria was a detection in the galaxy-wide IRAS-CS survey by Bronfman et al. (1996). In a few sources we found previously unknown secondary velocity components (see bottom part of Table 4). The CS(5-4) line and the corresponding $C^{34}S$ lines were found in large sub-samples (Table 4). A few sources show self-absorption effects (18089 – 1732, 18310 – 0825, 18337 – 0743, 18460 – 0307, 18488 + 0000 & 19217 + 1651) in the main isotopomer CS, but all other lines can be fitted well by Gaussian profiles. Table 4 presents the systemic velocity of each set of lines, the peak temperatures $T_{\rm mb}$, the integrated intensities $\int T_{\rm mb} dv$ and the line widths Δv of all detections.

We use a LVG-code to determine local gas densities and CS column densities within a beam of $\sim 22''$. For this purpose we use only sources for which 9 point maps were available to smooth the CS(5-4) and CS(3-2) lines spatially to the resolution of the (2–1) line. Additionally, we use for the LVG-calculations only sources with at least 3 different detected lines, because only line ratios can be used to determine physical parameters since the absolute line strengths are very unreliable due to the unknown beam filling factor. 61 sources fulfill these criteria for reasonable density and column density estimates. Schilke et al. (2001) note that for diatomic molecules line ratios cannot be used to determine the density or temperature independently but that the pressure $p = n \cdot T$ is constrained very well. We therefore calculate the LVG-models for 20, 40 and 80 K with gas densities of $10^4 - 10^6$ cm⁻³ and CS column densities of $10^{12} - 10^{16}$ cm⁻². We then performed χ^2 fits of our data to the LVG-model and calculated the incomplete gamma function as a goodness of fit estimator (Press et al. 1996). The 3σ levels of the incomplete gamma function were taken to derive the range of parameters our observations can be fitted with. Table 3 presents the derived thermal pressure p and the CS column density N(CS) for temperatures between 20 and 80 K. For cases where only single values are given the 3σ level of the incomplete gamma function revealed parameter ranges with errors of less than $10^{0.25}$. Sridharan et al. (2001) showed that temperatures derived from IRAS infrared observations are in the range of ~ 40 K while the rotation temperatures of NH₃ trace colder material around 20 K. Additional CH₃CN observations in a sub-sample indicate higher temperatures around 100 K. We estimate the gas density by assuming an average temperature of 40 K for the sample. The last two columns of Table 3 give the gas density range and CS column density range of possible parameters at 40 K.

For further statistical comparison we derive discrete parameters for the column and volume densities at 40 K: we take the mean value if ranges are given, the upper limits for CS column densities if $C^{34}S$ is a non-detection, and the lower limits in the density distribution if no upper limits for the gas density can be derived. To derive meaningful column densities those values have to be multiplied with the linewidth ($C^{34}S$ 2–1 if observed, else CS 2–1), because the LVG code gives column densities per km/s.

Figure (a) and (b) presents the gas density and CS column density distribution for the 61 sources we used in the calculations. The average local gas density is 1.0×10^6 cm⁻³ and the average CS column density is 1.3×10^{15} cm⁻². Additionally, we find that the CS abundance is independent of the core mass with an average value around 8×10^{-9} .

4. DISCUSSION

While the average gas densities we derive from the dust continuum emission are around 10^5 cm⁻³ the local gas densities implied by the CS observations are larger (up to one order of magnitude). Inhomogeneous density distributions are not unexpected because molecular clouds are clumped in all stages of molecular cloud evolution, from quiescent clouds in a pre-collapse phase (e.g. Beuther et 2000) to dense massive cores we are observing here (see also Stutzki 1989). Because CS is sensitive to the denser gas, the difference in both density determinations could also be explained simply by a density gradient of the core. However, as massive star formation is generally considered to proceed only in a clustered mode (Stahler et al. 2000) we favor the clumping as the most likely explanation (see also §4.1.2). Comparing our sample with hot cores and ultracompact HII regions UCHIIs (e.g. Kurtz et al. 2000) shows that HMPOs, UCHIIs and hot cores resemble each other in masses and column densities.

4.1. Implications from the radial profiles

It has to be stressed that in many sources the intensity profiles are not well fitted by single power laws (§3.3.2). Our approach using 3 parameters describes the intensity distribution significantly better: a steeper outer power law, a flatter inner power law and an inner breakpoint.

It has to be noted that although most descriptions of density profiles are expressed in terms of single power laws in low mass star formation research (§1), Ward-Thompson et al. (1999) find centrally flattened density profiles for a significant number of pre-stellar cores being in a state of evolution prior to protostars, whereas Alves et al. (2001) see a steeper outer region in one Bok globule modeled by Bonnor-Ebert spheres. Additionally, Motte & André (2001) found finite sizes for proto-stellar envelopes within clusters. A recent mid-infrared absorption study by Bac-(2000) revealed that inner flattening and outer steepening of pre-stellar low-mass cores occurs regularly. Henriksen et al. (1997) model pre-stellar cores by a centrally flattened hydrostatic core, an inner flatter power law distribution which is followed by a steeper outer power law distribution (essentially Bonnor-Ebert spheres), very similar to the results we obtain from our fits. In spite of the overall similarity of their model assumptions and our fitting results this is probably a chance coincidence since our sources most likely are cluster, whereas Henriksen et al. (1997) model single sources within clusters. But we like to stress that the intensity profiles Bacmann et al. (2000) derive for their low-mass pre-stellar cores are qualitatively similar to our results in the high-mass regime.

In the massive star formation regime Bonnell et al. (1998) model the accreting cores with shallow inner density distributions embedded in steeper outer regions. The outer steepening of the radial profiles is most likely due to the finite size and by that the finite mass-reservoir of the cores (Bacmann et al. 2000). Heaton et al. (1993) also found an inner region of constant molecular hydrogen density associated with the ultracompact HII region G34.3+0.2 (see also $\S4.1.2$). While in the low-mass regime there do exist a number of theoretical models predicting different pre-stellar intensity distributions than just one power law (e.g. Bonnor (1956); Basu & Mouschovias (1994); Henriksen et al. (1997)), theoretical high-mass research in that direction – especially the evolution of massive cores giving birth to whole cluster – has been rare so far and should be intensified in the future.

4.1.1. Different sub-groups and evolutionary effects

The distribution of inner radial profiles m_i (Fig. (a)) is broad, and we try to distinguish between the different parts of that distribution. Comparing the radial indices with other parameters such as luminosity, molecular observations (Sridharan et al. 2001), the mass and the CScolumn density, there are indications that the steeper indices correlate with the more luminous and more massive sources with high column densities, which show hot core signatures in molecular line observations and/or maser 2001). The flatter sources emission (Sridharan et al. might be divided into two sub-groups: one has adjacent resolvable cm-sources (Sridharan et al. 2001) indicating a more evolved state of evolution (Sridharan et al. 2001), where the evolving star has already disrupted the core (e.g. 22551+6221). The other sub-group with flat distributions is on the average less prominent in other tracers, they are less massive, mostly adjacent to the main cores, have lower column densities and show no other prominent star formation signature, particularly no cm-continuum.

To strengthen this hypothesis we select three subsamples and present them in Fig. (b): the first sub-sample shows CH₃OH and/or CH₃CN emission and has no or only hypercompact unresolved cm-emission features, the second sub-group shows resolvable (> 2") ultracompact HII regions, and the third consists of CH₃OH and CH₃CN non-detections, which have no or only hypercompact unresolved cm-emission (the molecular and cm data are taken from Sridharan et al. (2001)). The different groups are indicated in the last column of Table 2. We refrained from classifying adjacent sub-cores and those where no good molecular line or cm data were available. We are aware of the low-number statistic, thus we doubled the bin-size to increase the statistical significance. The first group, consisting of hot core type sources, has on the average steeper radial indices m_i (mean ~ 1.5) compared to the resolved cm-sources and the molecular line non-detections, which both have a mean radial index of ~ 1.1 .

We interpret the different sub-groups in Fig (b) in an evolutionary scenario: at the very early stages before or just at the beginning of star formation the profiles are rather flat with less pronounced gravitational centers and no or just weak internal heating (accretion and collapse begins). During the subsequent collapse and accretion phase before or at the very beginning of nuclear fusion the profiles are steepest due to strong accretion onto the central sources. After the first massive stars have formed in the cluster, they inject so much energy in the surrounding medium that the cores disrupt, which is observable by again flattening intensity distributions. Our sample consists of sources in all these stages and is therefore perfectly suited for further studies of different evolutionary stages.

4.1.2. The inner breakpoint

The third parameter we use to characterize the radial intensity profiles is the inner breakpoint of the power laws, from where on we model the emission on a constant level to the center. Similarly, Heaton et al. (1993) modeled the density distribution of the molecular gas associated with the ultracompact HII region G34.3+0.2 based on HCO⁺ and H¹³CO⁺ observations as approximately constant over the inner 0.1 pc ($\sim 5.5''$ at 3.8 kpc). For 2 sources (05358+3543 & 19217+1651) we have interferometric mm-continuum data from Plateau de Bure with approximately 3" resolution (to be published in a forthcoming paper, Beuther et al. 2001b, in prep). The massive cores are resolved into sources of sizes $\leq 5''$, and the nearby source 05358+3543 fragments into at least 3 massive sub-sources (distance ~ 1.8 kpc versus ~ 10 kpc for 19217+1651). The correspondence between the size of the sub-sources and the breakpoints of the power laws indicates that the breaking of the power laws is due to fragmentation of the cores. Each fragmented sub-core has its own substructure, but on a 11" scale, where we just see the emission integrated over the sub-cores, this appears as flattening. We investigated whether this flattening could be caused by increasing optical depth at small scales by integrating density power laws (derived from the intensity profiles, see section 4.1.3) along each line of sight, and find that the sources stay optically thin into the sub-arcsecond regime. This makes opacity effects very unlikely to explain the breakpoints.

Figure plots the corresponding linear distances from the peak position $b_{\rm lin}$ versus the derived core mass for sources without distance ambiguity. The linear distance from the peak, where the power law breaks increases with increasing mass (fitting results in approximately $b_{\rm lin} \propto M^{0.6}$). This seems to be plausible in the fragmentation scenario as well, because the more massive the cores are the larger and more massive the evolving clusters are expected to be (see also Sridharan et al. 2001), which leads to fragmentation on larger scales.

We excluded for the fit the three sources at the bottom (open circles) of Figure (05553+1631,18151-1208 and 19471+2641), because they clearly show a different behavior with a breakpoint below 0.5'', which means literally no breakpoint at all in our description. In the case of 19471+2641 cm-imaging snapshot-data (Sridharan et al. 2001) are very bad, but we think that extended emission is the cause of the data problems. This can explain the missing breakpoint easily because an ultracompact HII region has already destroyed the core sig-

nificantly, which is also indicated by the very filamentary structure of our 1.2 mm image. It is different in the cases of 05553+1631 and 18151-1208, which show both many signs of very early stages of massive star formation (Sridharan et al. 2001). Therefore we think that those sources are dominated strongly by one massive central objects, which makes fragmentation undetectable at our scales.

4.1.3. Density profiles

$$m = -1 + p + Q \cdot q + \epsilon_f \tag{1}$$

Q is a temperature and frequency dependent correction factor and equals ~ 1.2 at 1.2 mm and 30 K. The original equation 1 was derived for infinite power law distributions, but our steeper outer power laws indicate for a fraction of sources finite sizes. Those finite sizes have to be taken into account by a deprojection correction ϵ_f (Yun & Clemens 1991), but Motte & André (2001) showed that ϵ_f is small, roughly $\epsilon_f \leq 0.2$ if the outer edge is $\geq 20\%$ of the map size and even $\epsilon_f \leq 0.1$ if the outer edge is $\geq 30\%$ of the map size. In spite of possible errors this approach gives a first estimate on the density distribution. To derive the density index p we therefore need some knowledge about the temperature distribution. In the isothermal case the temperature does not depend on the distance to the peak, but in our cases of assumed centrally heated sources (accretion and/or stellar burning), the temperature decreases with distance to the source and Emerson (1988) shows that the power law index q of the temperature distribution can be approximated reasonably well by 0.4. We have additional 870 μ m maps for 13 of the sources, and comparison of the 870 μm and the 1.2 mm fluxes backs up the idea that the heating stems from the inside, at least for the main cores. Simulations of massive star forming regions (Osorio et al. 1999; v.d. Tak et al. 2000) revealed that in the inner regions (approximately < 2000 AU) steeper indices are expected. But outside the inner 2000 AU the temperature distribution flattens again and runs asymptotically into the usual $r^{-0.4}$ distribution (v.d. Tak et al. 2000). With our resolution being typically between 20000 and 50000 AU we can safely assume this asymptotic solution with q = 0.4 and derive the density power-law index p = 1.6, while the peak is at p = 1.8. As outlined by Motte & André (2001) we estimate the error in p to $\Delta p \sim \Delta m + \Delta q + 0.1 \sim 0.5$ with $\Delta m \sim 0.3$ and $\Delta q \sim 0.1$. We checked the derived density and temperature distributions by several DUSTY (Ivezic et al. 1999) and DIRT (Wolfire & Cassinelli 1986) radiative transfer program runs and got similar results to the straightforward deviation described above. The sources with very low m might not be centrally heated, yet, and by that a near isothermal temperature distribution is more likely (q < 0.4), thus their density indices are probably slightly larger.

Dividing the sample again in the same sub-groups of strong molecular emission sources, weak molecular emission sources and extended cm-emission sources (see section 4.1.1), the strong molecular sources have a mean density index of 2.0, the weak molecular sources 1.6 and the cm-sources 1.5.

As already mentioned, the standard theory of lowmass star formation from singular isothermal spheres (Shu 1977) predicts a power law index for the density distribution of r^{-2} in the static outer proto-stellar envelope. Theorist of high mass star formation propose a different, logatropic equation of state (Osorio et al. 1999; McLaughlin & Pudritz 1996) to explain e.g. the linewidth-size relation observed in molecular clouds. Those logatropic equations of state result in a different density distribution in the outer envelope, namely $n \propto r^{-1}$. The physical interpretation of the logatropic equation of state is under debate, but it is argued that in low mass star formation sites mainly thermal support works against collapse, while in massive sites non-thermal support is necessary. Recent observational work in molecular cores associated with well known ultracompact HII regions (UCHIIs) and hot cores argue in favor of density indices around 1.5 (Hatchell et al. 2000; v.d. Tak et al. 2000). But there do also exist observations of molecular gas associated with ultracompact HII regions, which favor density distributions similar to the low-mass case: e.g. independent studies of G34.3+0.2 in NH₃ and HCO^+ found density distributions around $r^{-1.9}$, respectively (Garay & Rodriguez 1990; Heaton et al. 1993).

The mean density index $p = 1.6 \pm 0.5$ derived for the inner density profile in our sample does not support strong deviation from the low-mass proto-stellar profiles studied by Motte & André (2001). The main difference between both studies is that Motte & André (2001) derive profiles for isolated low-mass proto-stellar envelopes and low-mass proto-stellar envelopes within clusters, while our sample presents the envelopes of massive star forming clusters. The evolutionary effects outlined in §4.1.1 with steepening density index in the strongest collapse and accretion phase and again flattening profiles, when the first ignited massive stars disrupt the molecular cores, indicate that with ongoing star formation turbulence gets more and more important. The steepest indices during the collapse and accretion phase resemble very much the structure known from isolated low-mass sources.

The density indices derived by Hatchell et al. (2000) and v.d. Tak et al. (2000) for well known hot cores associated with ultracompact HII regions favor more strongly the logatropic equations of state (1.0 < p < 1.5). They seem to correspond well with our flatter indices observed in more evolved cm-sources. To check that we applied our fitting procedure to the sources observed by Hatchell et al. (2000)¹. The average intensity index m derived by us for

¹ The data were kindly provided by Jennifer Hatchell.

those hot cores from 13.5" to 34.5" from the peak position is 1.5, resulting in density indices p around 1.9, which puts them in a similar category as the peaked sources of our sample and shows that the ultracompact HII regions have not disrupted the molecular cores significantly. The differences between the density indices derived in this two different ways, indicates how difficult it is to really constrain density distributions. The discrepancy might be explained to first order because Hatchell et al. (2000) describe their data by single power laws, while we argue that this is not sufficient. Especially, including the radial positions inside the beam into single power laws flattens the profiles because the power laws break at distances of a few arcsec from the center and the integrated emission continues more or less flat. But it has to be noted that Hatchell et al. (2000) fitted simultanously the SEDs, which puts additional constraints on the radial distributions.

We conclude that the analysis of density distributions is very dependent on model assumptions, and that comparisons of different data sets are only meaningful if they are analyzed using the same methods. Future approaches should try to incorporate different power laws or maybe Bonnor-Ebert spheres to describe the envelopes of massive star forming regions more properly, but that is out of the scope of this paper.

4.2. Line-width relations

The FWHM of Gaussian fits to the observed profiles give line information about the state of turbulence and the region where the gas is mainly emitting. Figure (a) plots the FWHM of $C^{34}S(2-1)$ versus $NH_3(1,1)$ and (2,2)linewidth (filled and open circles for a sub-sample of our HMPOs without distance ambiguities, see Sridharan et al. 2001) and a few molecular cores associated with UCHII regions (Churchwell et al. 1990; Cesaroni et al. 1991). The asterisks and triangles represent the NH_3 (1,1) and (2,2) lines, respectively. The HMPOs generally show a broader linewidth in $\rm C^{34}S$ than in NH₃ with an average ratio of $\frac{\Delta v({\rm C^{34}S})}{\Delta v({\rm NH_3})} \sim 1.5$. Similar linewidth differences are found in low mass dense cores (Zhou et al. 1989). Mapping of both lines by the same authors revealed that the average spatial extension of CS is larger than that of NH₃, which supports well known linewidth-size relations (Larson 1981). This is somewhat surprising since NH₃ traces less dense material than CS. For dark cores the effect seems to be due to the fact that CS is depleted in the dense cores while NH₃ is not, so the former traces the extended, more turbulent envelope, while the latter mostly traces the only thermally supported dense core. In our case, freezing out of CS is unlikely because of our high average temperatures, also our size scales are different. We propose that in our sources NH₃ traces the more quiescent medium density interclump gas, while CS emits mostly from the star forming and hence more turbulent cores.

The comparable database of 7 hot cores associated with UCHII regions (Churchwell et al. 1990; Cesaroni et al. 1991) is small but shows that the average linewidth of these hot cores is significantly higher than that of HMPOs (see also Sridharan et al. 2001). In few of the UCHII/hot core regions, where the linewidths are comparable, the ammonia abundance seems to be enhanced by grain mantle evaporation in hot cores, so NH₃ might trace those regions

as well.

How does the linewidth correlate with mass of the cores and state of evolution? Figure (b) presents the $C^{34}S(2-$ 1) linewidth at FWHM versus the core mass derived from the dust continuum data. The full circles show the HM-POs without distance ambiguity, while the asterisks and open squares present data from well known UCHII region associated hot cores. The latter $C^{34}S$ linewidth are taken from Cesaroni et al. (1991), and the masses for the hot cores are calculated from C³⁴S data (asterisks, Cesaroni et al. 1991) and from dust continuum or C¹⁷O observations (Hunter 1997; Hatchell et al. 2000, 1998). As full line we show the relation which is expected in case of virial equilibrium (see e.g. Myers 1999). While three hot cores are at the upper linewidth-end of the HMPOs, the majority of them lies far nearer the virial equilibrium track. Conversely, in our sample only the less massive objects correlate with the expected virial equilibrium correlation, whereas the more massive objects have significantly narrower linewidth and cluster in the plot below the hot core region. From an evolutionary point of view this seems to indicate that cores stay in virial equilibrium before the cores start collapsing, then with beginning star formation the whole massive core leaves the track of virial equilibrium and collapses violently until the first (massive) stars ignite and stabilize the overall collapsing motion at least partly by increasing the total luminosity. Accretion should still be possible at that stage of evolution but the overall collapse of the core is most likely stopped or at least slowed down. This effect of departure from the virial equilibrium track seems to be more prominent the more massive the cores become.

5. CONCLUSIONS

The presented database of 69 1.2 mm continuum maps of a homogenous sample of massive star-formation regions at very early stages of evolution sets many constraints on the physical parameters of high-mass proto-clusters.

The maps help disentangle many substructures, and it is obvious that a zoo of different morphologies is present. Calculations of total masses, column densities and densities show that HMPOs and hot cores associated with ultracompact HII resemble each other with regard to those parameters.

An analysis of the radial intensity profiles reveals that single power laws do not fit the data well, but that three parameters describe the radial profiles qualitatively better: a steeper outer power law, a flatter inner power law and an inner breakpoint, where the power law description stops, and we model the distribution as flat.

Larger scale maps will help to set better constraints on the outer envelope structure, but we propose that this steepening is due to the finite size of the cores as proposed in low-masses pre-stellar cores (Bacmann et al. 2000). Detailed theoretical models of the dust and gas envelopes of massive star forming regions are needed in the future. Comparing the inner breakpoints of the power law distributions with interferometric observations at higher resolution indicates that the breakpoints correspond to the separation and/or sizes of smaller sub-sources. Thus, most likely fragmentation causes the breaking of the power laws. Each individual sub-core might show other power law dis-

tributions, but this has to be investigated with much higher resolution (Beuther et al. in prep., Wyrowski et al. in prep).

Regarding the inner power law indices, we can divide the sources into three sub-samples: sources with strong molecular line emission, sources without strong molecular line emission or other strong star formation signposts and sources with extended cm-emission. While the first group has the steepest indices with a mean around 1.6 the other two groups have inner radial intensity indices m_i around 1.1. Therefore we propose an evolutionary scenario: star formation begins with very flat intensity distributions reflecting the initial conditions in molecular clouds, then during the strongest collapse and accretion phase the cores are very peaked with steep radial intensity distributions similar to those known from low mass scenarios, and finally when the first massive stars have ignited they inject so much energy into the surrounding molecular material that the cores disrupt and the intensity distributions flattens out again. Further support of this scenario is given by the C³⁴S linewidth which broadens for the hot core type sources significantly.

Deriving density distributions from the inner radial indices we get density power laws around $n \sim r^{-1.6\pm0.5}$, which is not very different from values found in low mass-cores (Shu 1977; Motte & André 2001). But regarding the large spread and the difficulties to constrain those density parameters tightly, stronger interpretations of the derived

density indices seem to be at least questionable.

CS and $C^{34}S$ observations were undertaken in different rotational lines. An LVG analysis leads to CS column density around 10^{15} cm⁻² and local gas densities around a few times 10^6 cm⁻³. The latter is higher than the average densities derived from the mm-continuum emission. This is expected because inhomogeneous density distributions, clumping and fragmentation of molecular gas is known to be an ubiquitous phenomenon in molecular clouds.

Comparing linewidth-mass relations of our sample with more evolved ultracompact HII regions from the literature indicate that massive cores are near virial equilibrium before the collapse phase, then with starting star formation they leave the virial equilibrium track and collapse violently until the first massive stars ignite which starts to stabilize the cores again at least partly.

We are indebted to Robert Zylka for providing and helping with the MOPSI software. We like to thank Frank Bertoldi a lot, who did most of the MAMBO observations at Pico Veleta. Additionally, we thank Bernd Weferling for conducting parts of the MAMBO observations as well. Data of ultracompact HII regions were kindly provided by Jenny Hatchell. H. Beuther gets support by the *Deutsche Forschungsgemeinschaft*, *DFG* project number SPP 471. F. Wyrowski is supported by the National Science Foundation under Grant No. AST-9981289.

Larson R.B., 1981, MNRAS, 194, 809

Lis D., Serabyn E., Keene J., et al., 1998, ApJ, 509, 299

REFERENCES

Adams F., 1991, ApJ, 382, 544
Alves J.F., Lada C.J., Lada E.A., 2001, Nature, vol. 409, p. 159
Bacmann A., Andre P., Puget J.-L., et al., 2000, A&A, 361, 555
Basu S., Mouschovias T.C., 1994, ApJ, 432, 720
Beuther H., Kramer C., Deiss B., Stutzki J., A&A, 2000, 362, 1109
Bonnell I.A., Bate M.R., Zinnecker H., 1998, MNRAS, 298, 93
Bonnor W.B., 1956, MNRAS, 116, 351
Bronfman L., Nyman L.A., May J., 1996, A&AS, 115, 81
Bronfman L., Casassus S., May J., Nyman L.-A, 2000, A&A, 358, 521
Broguière D., Neri R., Sievers A., 1995, NIC bolometer user's guide (IRAM internal report)
Cesaroni R., Walmsley C.M. Kömpe C., Churchwell E., 1991, A&A, 252, 278
Cesaroni R., Curchwell E., Hofner P., Walomsley C., Kurtz S., 1994, A&A, 288, 903
Churchwell E., Walmsley C., Cesaroni R., 1990, A&ASS, 83, 119
Emerson E.T., Klein U., Haslam C.G.T., 1979, A&A, 76, 92
Emerson J.P., 1988, in: Formation and Evolution of Low Mass Stars, ed. Dupree & Lago, 21
Frerking M., Langer L., Wilson R., 1982, ApJ, 262, 590
Garay G., Rodriguez L.F., 1990, ApJ, 362, 191
Gregory P., Condon J., 1991, ApJS, 75, 1011
Griffith M., Wright A., Burke B., Ekers R., 1994, ApJS, 90, 179
Hatchell 1998, Thompson M.A., Millar T.J., MacDonald, G.H., 1998, A&AS, 133, 29
Hatchell J., Fuller G., Millar T., Thompson M., MacDonald G., 2000, A&A, 357, 637
heaton B.D., Little L.T. Yamashita T., et al., 1993, A&A, 278, 238
Henriksen R., Andre P., Bontemps S., 1997, A&A, 323, 549
Hildebrand R., 1983, Q. Jl. R. astr. S., 24, 267
Hunter T., 1997, Ph.D. Thesis, Caltech
Hunter T., Churchwell E., Watson C., Cox P., Benford D., Roelfsema P., 2000, AJ, 119, 2711
Ivezic Z., Nenkova M., Elitzur M., 1999, User manual for DUSTY,

University of Kentucky Kreysa E., Gemünd H.P., Gromke J., et al. 1998, Proc. SPIE, 3357,

Kurtz S., Cesaroni R., Churchwell E., Walmsley M., 2000, in Protostars & Planets IV, ed. V. Mannings

McLaughlin D., Pudritz R., 1996, ApJ, 469, 194 Mezger P., Wink J., Zylka R., 1990, A&A, 228, 95 Molinari S., Brand J., Cesaroni R., Palla F., Palumbo G., 1998, A&A, Molinari S., Brand J., Cesaroni R., Palla F., 2000, A&A, 355, 617 Motte F., Ándré P., 2001, A&A, 365, 440 Mundy L.G., Looney L.W., Welch W.J., 2000, in Protostars & Planets IV, ed. V. Mannings
Myers P., Fuller G., 1992, ApJ, 396, 631; Myers P.C., 1999, in: The Physics of Star Formation and Early Stellar Evolution, eds. C.J. Lada & N. Kylafis, Dordrecht: Kluwer Olmi L., Felli M., 1998, A&A, 339, 872
Osorio M., Lizano S., D'Alessio P., 1999, ApJ, 525, 808
Ossenkopf V., Henning Th., 1994, A&A, 291, 943
Press W.H., Teukolsky S.A., Vetterling W.T., Flannery B.P., 1996, Numerical Recipes, 2. Edition, Cambridge University Press Schilke P., Pineau de Forets G., Walmsley C.M., Martin-Pintado J., A&A, 2001, accepted Shu F., 1977, ApJ, 214, 488 Shu F., Adams F., Lizano S., 1987, ARA&A 25, 23 Sridharan T.K., Beuther H., Schilke P., Menten K., Wyrowski F., Stahler S., Palla F., Ho P., 2000, in Protostars & Planets IV, The University of Arizona Press Stutzki J., 1989, ARAA, volume 27 Terebey S., Chandler C., Andre P., 1993, ApJ, 414, 759 van der Tak F., van Dishoek E., Evans N., Blake G., 2000, ApJ, 537, Ward-Thompson D., Motte F., André P. 1999, MNRAS, 305, 143 Whitworth A., Summers D., 1985, MNRAS, 214,1 Wolfire M.G. Cassinelli J.P., 1986, 310, 207 Wright A., Griffith M., Burke B., Ekers R., 1994, ApJS, 91, 111 Yun J.L., Clemens D.P., 1991, ApJ, 381, 474 Zhou S., Wu Y., Evans N.J., Fuller G.A., Myers P.C., 1989, ApJ, 346, 168 Zylka R., 1998, Pocket Cookbook for the MOPSI Software, MPIfR internal report

Table 1
Observing parameters

line	freq	HPBW	T_{sys}	resolution	
	[GHz]	["]	[K]	$[\mathrm{km/s}]$	
CS 2–1	97.98	27	120	0.5	
CS 3-2	146.97	17	380	0.3	
CS 5-4	244.94	11	570	0.4	
$C^{34}S$ 2-1	96.41	27	370	0.5	
$C^{34}S$ 3-2	144.62	17	970	0.3	
$C^{34}S$ 5-4	241.02	11	1220	0.2	

source	#	$_{\rm mJy/(11'')^2}^{\rm peak}$	int. flux	$\Delta \mathbf{x}$ ["]	Δy ["]	maj	min ["]	PA	type	
05358 + 3543	1 2	887 (19) 272 (5)	6.0 0.6	27.5 (0.3) 5.5 (0.3)	33.3 (0.3) 45.7 (0.5)	26.7 (0.6) 46.0 (0.8)	19.8 (0.8) 18.1 (2.4)	45 31	1 0	
	3	166 (2) 231 (6)	0.4 1.0	-19.8 (0.6) 8.8 (0.6)	83.9 (0.6) -0.8 (0.6)	$47.2 \stackrel{()}{(} 0.5 \stackrel{)}{)}$ $33.6 \stackrel{()}{(} 2.0 \stackrel{)}{)}$	19.4 (2.8) 29.6 (1.6)	45 45	0	
05490 + 2658	1 2	176 (3) 186 (5)	1.3	-7.8 (0.4) $-17.3 (0.6)$	4.4 (0.8) 58.8 (0.7)	43.9 (1.0) 48.3 (1.7)	27.8 (2.4) 34.2 (2.5)	5 21	3	
05553+1631	1	317 (4) 2134 (37)	1.3	-3.1 (0.2) 3.2 (0.2)	-2.6(0.2)	21.5 (0.6) 11.4 (0.4)	16.5 (0.3)	48	1 1	
18089-1732	2	259 (3)	5.1 0.9	-14.8 (0.6)	0.1 (0.2) 0.2 (0.2)	85.8 (4.7)	8.9 (0.4) 20.2 (0.6)	-72 69	0	
	3 4	112 (2) $292 (12)$	$0.3 \\ 0.8$	-84.2 (0.5) 39.1 (0.2)	$49.3 \; (\; 0.5 \;) \\ 90.0 \; (\; 0.3 \;)$	35.5 (1.7) 17.7 (0.7)	27.3 (1.0) 11.2 (1.0)	$-65 \\ -17$	0	
18090 - 1832	$\frac{1}{2}$	276 (4) 79 (4)	$0.6 \\ 0.2$	-0.4 (0.2) $16.1 (0.5)$	$\begin{array}{c} 1.2 \; (\; 0.2 \;) \\ 32.8 \; (\; 0.5 \;) \end{array}$	$12.3 \; (\; 0.4 \;) \\ 14.4 \; (\; 1.3 \;)$	11.3 (0.4) $13.6 (1.0)$	6 79	0	
18102 - 1800 $18151 - 1208$	1 1	316 (1) $672 (24)$	$\frac{3.3}{3.6}$	-10.7 (0.1) 13.2 (0.4)	-23.9 (0.1) -4.9 (0.3)	69.4 (0.3) 26.7 (1.1)	39.7 (0.1) 15.8 (0.7)	$-32 \\ -62$	2 1	
	2	424 (9) 149 (3)	2.6 0.9	-98.9 (0.3) -72.3 (0.4)	-32.8 (0.3) 26.5 (0.5)	29.8 (0.9) 36.4 (0.9)	22.0 (0.7) 24.0 (1.2)	$-46 \\ -25$	1 0	
18159-1550	4	51 (7) 109 (2)	$0.2 \\ 1.1$	$10.4 \stackrel{()}{(} 0.6 \stackrel{()}{)}$ $12.0 \stackrel{()}{(} 0.6 \stackrel{()}{)}$	92.6 (0.1) -7.7 (0.1)	39.8 (0.8) 51.8 (0.6)	24.6 (2.9) 47.1 (0.6)	$-45 \\ -25$	0 2	
$18182\!-\!1433$	$\frac{1}{2}$	1303 (3) 100 (2)	3.9 0.3	19.0 (0.1) 101.2 (0.7)	4.2 (0.1) $-72.9 (0.9)$	$13.0 \stackrel{()}{(} 0.1 \stackrel{()}{)} 42.7 \stackrel{()}{(} 2.6 \stackrel{()}{)}$	$11.5 \stackrel{()}{(} 0.1 \stackrel{)}{)}$ $21.3 \stackrel{()}{(} 1.0 \stackrel{)}{)}$	$-86 \\ -45$	1 0	
$18223\!-\!1243$	1 2	328 (6)	2.5	-5.4 (0.2)	-8.8(0.4)	48.7 (0.6) 55.8 (0.4)	22.0 (1.3)	-12	2	
	3	124 (2) 205 (1)	0.6 0.8	-19.9 (0.3) $-38.5 (0.2)$	-118.4 (0.7) $-190.5 (0.3)$	39.9 (0.2)	14.5 (2.1) 10.7 (0.8)	-15 -20	0	
$18247\!-\!1147$	4 1	52 (2) 560 (11)	0.3 1.9	-53.7 (1.1) 8.7 (0.1)	-337.2 (1.3) -0.2 (0.2)	59.2 (1.0) 16.3 (0.3)	$16.1 \ (\ 4.7\) \ 11.7 \ (\ 0.4\)$	-34 2	0	
	2 3	113 (3) 85 (3)	$0.5 \\ 0.4$	$^{12.4}_{-21.4}$ ($^{0.3}_{1.0}$)	$40.2 \; (0.5) \\ 74.8 \; (0.6)$	$38.8 \; (0.8) \\ 49.3 \; (4.6)$	$19.8 \; (\; 1.8 \;) \\ 24.2 \; (\; 1.2 \;)$	$^{-14}_{-57}$	0	
$18264\!-\!1152$	4 1	182 (2) 1769 (42)	0.9 7.9	-84.7 (0.2) $5.1 (0.2)$	-63.7 (0.1) 3.7 (0.2)	24.8 (0.2) 16.6 (0.5)	22.9 (0.3) 14.1 (0.4)	-80	0 1	
18272 - 1217	$\frac{1}{2}$	141 (5) 119 (3)	$0.6 \\ 0.3$	$2.4\ (0.3\) \\ -5.4\ (0.4\)$	10.1 (0.3) -13.7 (0.1)	24.0 (1.0) 20.9 (1.4)	18.7 (0.9) 18.8 (1.9)	$-69 \\ -87$	2 0	
$18290\!-\!0924$	1 2	420 (15) 442 (17)	1.4 1.9	-12.9 (0.4) $22.6 (0.4)$	-4.3 (0.6) -13.6 (0.6)	22.3 (1.0) 18.7 (1.1)	16.9 (2.0) 17.3 (2.1)	$-14 \\ -20$	2	
$18306\!-\!0835$	1 2	731 (0) 212 (8)	3.2 0.6	32.1 (0.1) -68.5 (0.1)	7.1 (0.1) 12.4 (0.1)	19.4 (0.1) 13.2 (0.7)	16.2 (0.1) 12.4 (0.3)	-1 2	0	
18308 0041	3	103 (2) 554 (10)	0.8	153.1 (0.6)	69.5 (0.9) 6.9 (0.3)	52.6 (1.0) 19.1 (0.6)	28.4 (2.2)	-14	3	
18308-0841	2	203 (6)	2.5 0.6	17.3 (0.2) 25.8 (1.4)	29.0 (1.3)	46.8 (3.9)	15.7 (0.5) 15.8 (0.8)	-45	0	
	3	100 (1) 75 (1)	0.7 0.2	-32.1 (0.4) -71.0 (0.2)	51.6 (0.4) 25.1 (0.2)	52.2 (0.4) 21.2 (0.6)	19.8 (1.5) 17.0 (0.5)	44 45	0	
$18310\!-\!0825$	5 1	$62 (2) \\ 235 (5)$	0.2 3.6	$41.7 \; (\; 0.6 \;) \\ 10.9 \; (\; 0.5 \;)$	$104.3 (0.9) \\ -10.6 (0.5)$	49.7 (0.9) 51.4 (1.4)	$16.6 \; (\; 4.0 \;) \\ 41.5 \; (\; 1.2 \;)$	$-30 \\ 45$	0	
	2	325 (9) 137 (4)	1.3 0.6	-47.1 (0.4) -74.5 (0.6)	135.4 (0.4) 119.3 (0.4)	28.4 (1.1) 23.5 (1.0)	17.5 (0.8) 22.2 (0.8)	$-45 \\ -69$	0	
	4	126 (8) 90 (4)	$0.5 \\ 0.3$	-115.5 (1.0) -45.9 (0.7)	144.6 (0.9) -105.8 (0.5)	34.4 (3.4) 33.5 (2.8)	20.4 (2.0) 19.3 (1.2)	$-48 \\ -66$	0	
$18337\!-\!0743$	1 2	485 (1) 180 (2)	5.0 1.1	179.0 (0.1) -18.8 (0.1)	73.1 (0.2)	43.1 (0.2) 37.9 (0.8)	23.5 (0.4) 22.1 (0.1)	$\frac{13}{-45}$	0	
19945 0641	3	110 (3)	0.3	-160.1 (0.3)	-28.1 (0.3)	19.9 (1.0)	8.5 (0.5)	-56	0	
18345 - 0641 $18348 - 0616$	1	265 (1) 249 (3)	1.4	$3.3 \ (0.1)$ $76.6 \ (0.3)$	1.3 (0.2) 8.0 (0.3)	29.0 (0.9) 39.9 (0.6)	21.5 (1.3) 29.1 (0.6)	44 45	3	
	2 3	126 (2) 120 (2)	$0.5 \\ 0.5$	39.9 (1.0) 0.3 (0.5)	$9.2 \; (\; 0.4 \;) \\ 75.3 \; (\; 0.6 \;)$	49.9 (3.2) 36.7 (1.8)	35.6 (1.5) 32.5 (1.3)	85 45	0	
	4 5	54 (1) 108 (4)	$0.4 \\ 0.3$	-59.0 (0.1) $6.1 (0.5)$	-51.2 (0.1) -138.4 (0.6)	68.0 (3.9) 26.0 (1.4)	34.9 (0.5) 21.0 (1.5)	$\frac{54}{24}$	0	
	6 7	97 (1) 90 (2)	0.3 0.4	7.8 (0.4) $-11.1 (0.8)$	-113.3 (0.3) -179.0 (0.6)	43.6 (2.9) 43.7 (2.2)	19.6 (0.8) 27.5 (1.3)	$-45 \\ 73$	0	
18372 - 0541 $18385 - 0512$	1 1	260 (4) 716 (8)	$\frac{1.4}{2.1}$	-0.2 (0.1) 19.7 (0.1)	2.0 (0.1) $4.9 (0.1)$	$30.3 \; (\; 0.4 \;) \\ 13.2 \; (\; 0.3 \;)$	19.6 (0.8) 12.7 (0.2)	30 45	0	
	2	78 (1) 67 (1)	0.5 0.3	109.5 (0.5) 79.7 (0.2)	48.7 (0.4) -58.1 (0.4)	59.4 (2.2) 35.6 (0.4)	35.1 (0.8) 17.1 (1.0)	$-51 \\ -16$	0	
18426 - 0204 $18431 - 0312$	1	67 (1) 143 (1)	1.1 1.1	-14.3 (0.1) -16.9 (0.3)	-2.1 (0.1) 3.0 (0.3)	100.6 (1.2) 32.1 (0.9)	71.3 (0.1) 31.0 (0.5)	$64 \\ -45$	0 2	
	2	140 (1)	0.7	-98.1 (0.1)	-120.6 (0.4)	36.4 (0.6)	16.5 (1.5)	-36	0	
18437 - 0216	1 2	135 (2) 57 (1)	0.9 0.3	-5.4 (0.3) $11.6 (1.0)$	$-47.8 (0.6) \\ -1.4 (0.9)$	55.0 (0.6) 48.4 (7.5)	$24.9 (2.5) \\ 33.5 (0.5)$	-5 45	0	
	3 4	$\begin{array}{c} 91 \ (1) \\ 72 \ (1) \end{array}$	$0.3 \\ 0.3$	$^{-12.0}$ ($^{0.3}$) $^{1.9}$ ($^{0.6}$)	$60.3 (0.3) \\ -112.8 (0.5)$	26.7 (1.1) 37.7 (1.9)	18.1 (0.6) 25.1 (1.1)	60 67	0	
	5 6	69 (2) 141 (10)	$0.3 \\ 0.3$	40.7 (0.4) $-89.7 (0.6)$	-126.5 (0.6) -134.3 (0.7)	32.4 (1.2) 11.8 (0.8)	25.7 (1.6) 9.7 (1.2)	0 3	0	
18440 - 0148 $18445 - 0222$	1 1	120 (5) $257 (4)$	$0.5 \\ 1.7$	3.9 (0.6) $-8.7 (0.1)$	1.8 (0.5) 20.5 (0.3)	23.4 (1.2) 36.7 (0.7)	17.5 (1.2) 32.5 (1.0)	-36	0 2	
	2	69 (2) 119 (4)	0.3 0.5	58.1 (0.8) -46.3 (0.1)	$-84.1 \stackrel{()}{(} 0.7 \stackrel{)}{)}$ $-140.5 \stackrel{()}{(} 0.4 \stackrel{)}{)}$	46.7 (3.3) 32.2 (1.3)	$24.2 \stackrel{()}{(}1.7 \stackrel{)}{)}$ $22.4 \stackrel{()}{(}1.1 \stackrel{)}{)}$	-52 80	0	
$18447\!-\!0229$	1 2	98 (2) 99 (5)	$0.7 \\ 0.2$	$-31.1 \ (0.5)$ $12.1 \ (0.3)$	-11.2 (0.5) -140.2 (0.4)	39.7 (1.3) 16.3 (0.7)	38.2 (1.3) 5.2 (1.1)	$-7 \\ -22$	0	
$18454\!-\!0136$	1 2	298 (7) 161 (2)	1.1 0.5	-18.6 (0.3) $-14.4 (0.3)$	-3.5 (0.2) -157.8 (0.2)	21.6 (0.9) 19.4 (0.6)	13.6 (0.5) 13.5 (0.6)	$-74 \\ 73$	0	
$18454\!-\!0158$	1 2	157 (3) 130 (5)	0.4 0.4	11.5 (0.3) -19.6 (0.3)	52.7 (0.3) 44.7 (0.4)	16.8 (0.5) 20.8 (1.0)	16.4 (0.6) 18.5 (1.3)	$-74 \\ -9$	0	
	3	199 (9)	0.7	-81.1 (0.5)	73.8 (0.5)	22.1 (1.0)	19.1 (1.2)	-45	0	
	4 5	261 (43) 90 (3)	0.4 0.3	2.0 (0.7) $-48.2 (0.4)$	132.2 (0.9) -81.4 (0.4)	20.3 (0.8) 35.2 (1.5)	2.2 (2.5) 9.0 (0.6)	77 -45	0	
40400	6 7	102 (5) 92 (8)	0.1 0.2	14.8 (0.3) $-133.8 (0.1)$	-54.6 (0.3) -15.4 (0.6)	13.1 (0.7) 34.9 (0.8)	11.0 (0.4)	52 13	0	
18460 - 0307	$\frac{1}{2}$	162 (3) 95 (1)	$0.9 \\ 0.4$	$11.9 (0.4) \\ -15.5 (0.7)$	-2.8 (0.3) $4.6 (0.3)$	36.3 (1.2) 41.2 (2.5)	$23.1 (0.7) \\ 24.8 (0.8)$	$-53 \\ 79$	0	
	3	71 (1) 173 (4)	$0.3 \\ 0.3$	-44.3 (0.9) 111.2 (0.2)	$7.0 \stackrel{(}{(} 0.2 \stackrel{)}{)}$ $-109.2 \stackrel{(}{(} 0.2 \stackrel{)}{)}$	50.4 (2.6) 10.3 (0.5)	23.1 (0.6) 6.0 (0.4)	88 73	0	
18470-0044	5 1	45 (1) 465 (6)	0.5 1.5	120.2 (0.7) 16.6 (0.1)	11.8 (0.1) 3.9 (0.1)	70.4 (1.3) 17.0 (0.7)	49.3 (0.3) 12.1 (1.0)	$-45 \\ 23$	0	
18472 - 0022	1 2	276 (5) 80 (2)	2.7 0.3	26.2 (0.3) 42.9 (0.3)	13.0 (0.3) -39.0 (0.5)	33.5 (1.0) 48.8 (1.3)	27.9 (0.8) 32.0 (3.1)	-84 40	0	
18488+0000	3	83 (2) 393 (7)	0.2 2.2	51.5 (0.3) 12.1 (0.4)	-62.0 (0.8) -12.5 (0.5)	48.5 (1.1) 24.2 (1.5)	28.1 (4.4) 23.1 (1.2)	12 -8	0 2	
18517+0437	2	168 (2)	0.4	-4.2(0.4)	$9.8 \; (\; 0.5 \;)$	29.0 (0.6)	15.0 (2.0)	28	0	
	2	812 (2) 138 (3)	7.2 0.5	7.8 (0.1) $-30.2 (2.5)$	7.7 (0.1) 25.7 (1.5)	30.8 (0.3) 54.1 (12.1)	27.4 (0.2) 33.9 (5.2)	-47 82	0	
18521 + 0134 $18530 + 0215$	1	234 (7) 598 (2)	1.0 5.6	-0.6 (0.2) -3.6 (0.1)	$3.0 (0.3) \\ -0.7 (0.1)$	18.2 (0.6) 46.0 (0.4)	14.8 (0.8) 25.0 (0.3)	-69	0	
18540 + 0220 $18553 + 0414$	1 1	69 (1) 492 (5)	$0.7 \\ 1.9$	$15.2 \ (0.1)$ $7.0 \ (0.1)$	-7.7 (1.0) 9.7 (0.1)	$62.4 \; (\; 0.9 \;) \\ 17.7 \; (\; 0.2 \;)$	$24.5 \ (1.1) \ 12.8 \ (0.4)$	41 6	2 2	
18566 + 0408 $19012 + 0536$	1 1	486 (10) 395 (3)	1.6 1.5	$\begin{array}{c} 1.8 \; (\ 6.0\) \\ 4.2 \; (\ 0.1\) \end{array}$	$0.7 \; (\; 6.0 \;) \\ 2.7 \; (\; 0.1 \;)$	20.0 (6.0) 19.1 (0.5)	$12.0 \stackrel{(}{(} 6.0 \stackrel{)}{)} $ $13.0 \stackrel{(}{(} 0.3 \stackrel{)}{)}$	$\frac{49}{71}$	1 0	
19035 + 0641 $19074 + 0752$	1	312 (4) 129 (1)	2.6 0.8	$7.4\ (\ 0.3\) \\ 6.4\ (\ 0.2\)$	7.9 (0.2) $-6.4 (0.4)$	33.9 (0.5) 54.4 (0.8)	29.7 (1.0) 34.3 (0.9)	$-17 \\ -5$	0	
19175+1357	1 2	141 (8) 87 (4)	0.5 0.1	1.8 (0.1) -6.8 (0.4)	0.8 (0.2) -17.2 (0.4)	16.4 (0.9) 17.1 (1.1)	15.6 (0.7) 8.5 (0.7)	36 -53	0	
	3 4	50 (1) 78 (1)	0.1 0.2 0.2	42.8 (0.3) 21.5 (0.3)	-55.0 (0.5) -83.6 (0.3)	37.0 (0.6) 25.1 (1.3)	14.2 (2.2) 14.4 (0.7)	-23 -45	0	
	4	10 (1)	0.2	21.0 (0.3)	-65.0 (0.5)	20.1 (1.3)	14.4 (0.7)	-40	U	

Table 2—Continued

	5	63 (1)	0.2	7.1 (0.5)	-97.3(0.2)	38.7 (1.9)	17.2 (0.6)	-73	0
	6	58 (0)	0.4	-111.9 (0.8)	-82.0 (0.4)	89.1 (2.8)	26.5 (0.5)	66	0
	7	39 (0)	0.2	58.0 (0.5)	69.6 (0.3)	35.4 (1.2)	18.9 (0.8)	77	0
19217 + 1651	1	640 (3)	2.6	-0.4(0.1)	7.8 (0.1)	18.0 (0.3)	15.1 (0.3)	-10	1
19220 + 1432	1	256 (4)	1.9	5.1 (0.5)	0.6 (0.2)	44.1 (0.7)	20.3 (0.5)	83	2
19266 + 1745	1	323 (15)	1.3	24.5 (0.5)	5.9 (0.6)	23.3 (1.0)	16.8 (1.7)	14	3
	2	121 (3)	0.3	98.2 (0.3)	-48.8(0.3)	15.7 (0.7)	12.5 (0.7)	-68	3
19282 + 1814	1	273 (23)	1.0	-71.0(0.6)	-28.5(0.1)	25.2 (1.6)	18.0 (1.8)	87	0
19403 + 2258	1	90 (0)	1.7	17.2 (0.2)	-10.6(0.2)	108.7 (0.6)	70.6 (0.6)	-45	0
19410 + 2336	1	849 (19)	6.3	-6.8(0.3)	4.0 (0.3)	26.3 (0.8)	23.8 (0.7)	-54	1
	2	239 (5)	1.4	-16.4(0.4)	57.0 (0.8)	42.7 (0.9)	27.9 (1.8)	-5	1
19411 + 2306	1	222 (3)	1.3	-1.5(0.2)	0.5(0.2)	26.7 (0.4)	22.7 (0.5)	45	0
	2	97 (1)	1.0	-55.3(0.3)	-12.7 (0.6)	57.5 (1.4)	41.8 (2.2)	0	0
19413 + 2332	1	139 (2)	1.2	5.4 (0.3)	13.5 (0.2)	38.7 (1.2)	20.9 (0.5)	-77	0
	2	69 (1)	0.4	-35.1 (0.6)	17.8 (0.4)	38.0 (1.9)	27.0 (1.0)	61	0
19471 + 2641	1	171 (6)	0.4	61.5~(~0.3~)	77.8 (0.4)	19.7 (1.4)	12.7 (0.8)	-45	0
	2	63 (3)	0.2	44.7 (0.8)	117.5 (0.7)	29.8 (1.2)	15.4 (2.6)	44	0
20051 + 3435	1	167 (1)	1.3	11.4 (0.1)	10.3 (0.1)	60.5 (0.1)	32.8 (0.1)	28	0
20081 + 2720	1	180 (4)	0.6	21.6 (0.4)	-49.0 (0.2)	32.1 (1.2)	15.8 (0.5)	84	0
	2	61 (1)	0.1	35.3 (0.2)	77.2 (0.3)	13.0 (0.4)	11.0 (0.8)	14	0
	3	46 (1)	0.1	92.9 (0.1)	-109.1 (0.1)	18.8 (1.1)	8.9 (0.6)	62	0
20126 + 4104	1	1087 (29)	5.8	-1.5(0.2)	2.0 (0.2)	19.0 (0.6)	17.0 (0.6)	8	1
20205 + 3948	1	104 (1)	0.9	-11.8(0.1)	10.0 (0.1)	74.7 (1.8)	27.6 (0.6)	66	3
	2	54 (2)	0.3	29.2 (0.9)	-7.1(0.9)	48.5 (1.6)	32.4 (3.8)	45	0
20216 + 4107	1	264 (4)	1.6	-2.9(0.2)	-1.9(0.2)	27.1 (0.5)	19.0 (0.7)	45	3
20293 + 3952	1	354 (0)	4.2	23.0 (0.1)	3.4 (0.1)	58.9 (0.2)	39.7 (0.1)	71	2
	2	102 (1)	0.7	-14.0 (0.7)	31.2 (1.8)	52.8 (1.1)	38.8 (4.5)	22	o
20319 + 3958	1	214 (4)	1.4	-2.7(0.1)	-10.1(0.1)	31.8 (0.1)	22.2 (0.5)	7	2
20332+4124	1	265 (3)	3.5	-8.7(0.4)	1.4 (0.3)	29.1 (1.3)	27.3 (0.7)	86	2
20343 + 4129	1	313 (3)	1.6	9.5 (0.2)	-4.3 (0.2)	31.9 (0.8)	21.9 (0.4)	64	3
	2	296 (3)	1.0	-3.2 (0.4)	-3.9 (0.2)	30.9 (1.3)	17.9 (0.5)	89	0
004041 #004	3	123 (3)	0.7	-34.2 (1.2)	-14.4 (0.5)	37.2 (3.4)	24.0 (1.5)	-74	0
22134+5834	1	229 (1)	2.5	3.2 (0.1)	-3.0 (0.1)	53.4 (0.2)	30.4 (0.3)	45	3
22551+6221	1	101 (1)	2.1	12.4 (0.6) -8.6 (0.3)	-21.7 (0.5) -8.8 (0.3)	51.6 (2.8) 32.4 (0.9)	38.1 (1.2)	58	2 2
22570 + 5912	$\frac{1}{2}$	215 (4) $157 (11)$	0.9	-8.6 (0.3) -55.7 (0.4)	-8.8 (0.3) -52.4 (0.4)	24.2 (1.7)	29.8 (0.7) 23.5 (1.2)	$-45 \\ 13$	0
	3	66 (1)	0.5	-86.5 (1.1)	4.6 (0.4)	47.7 (4.5)	32.4 (1.9)	71	0
	4		1.0	-86.5 (1.1) -129.7 (0.9)	21.0 (0.6)	44.8 (2.6)		45	0
23033+5951	1	86 (3) 631 (16)	3.5	-129.7 (0.9)	-1.7 (0.3)	24.8 (2.6)	38.8 (3.8) 14.6 (0.8)	-25	0
23033+5951 23139+5939	1	530 (7)	2.3	-2.9 (0.2) 8.7 (0.1)	-1.7 (0.3) 5.5 (0.1)	24.8 (0.5) 21.3 (0.4)	15.0 (0.4)	-25 30	1
23159+5939 $23151+5912$	1	406 (11)	2.0	0.2 (0.2)	-0.5 (0.1)	16.5 (0.4)	14.4 (0.7)	33	3
23151+5912 $23545+6508$	1	148 (3)	0.9	3.2 (0.7)	-0.5 (0.2) -20.6 (0.8)	35.4 (2.3)	30.9 (2.1)	12	3
23040+0308	2	153 (2)	0.9	-17.6 (0.3)	-34.9 (0.3)	27.4 (0.9)	24.8 (0.7)	-73	0
	- 2	153 (2)	0.7	-17.0 (0.3)	-34.9 (0.3)	21.4 (0.9)	24.0 (0.7)	-73	U

Note. — Presented are the peak flux, the integrated flux, the positional offsets, the major and minor axes of the 2-dimensional Gaussian fits and the position angle. The last column shows the three sub-groups as outlined in §4.1.1. 0: no grouping, 1: CH₃OH and/or CH₃CN detections and no resolved cm-source, 2: resolved cm-emission, 3: no CH₃OH and CH₃CN emission and no resolved cm-source (Sridharan et al. 2001)

 $\label{eq:Table 3} \text{Results from the } 1.2 \text{ mm and CS data}$

						RESULI	5 FROM	1 1111	11.4		ир Съ Б				
source 05358+3543	#	$\frac{M_{ m far}}{613}$	$M_{ m near}$	Ngas 5.8	A _V 617	n_{far} 9.3	n_{near}	$\frac{m_i}{1.4}$	m _o	5.5	$\frac{p}{7.0-7.5}$	N(CS) 14.25-15.0	$\frac{^{\mathrm{n}}40K}{5.5-6.0}$	$N_{40K}(CS)$ 14.5-14.75	
	2	57 41	-	1.8	191	2.1	_	-	-	_	_	_	_	_	
	4	102	_	$\frac{1.1}{1.5}$	$\frac{117}{159}$	$\frac{1.2}{1.8}$	_	_	_	_	_	=	=	_	
05490 + 2658	$\frac{1}{2}$	195 165	_	$\frac{1.2}{1.3}$	$\frac{127}{138}$	$\frac{1.1}{1.0}$	_	$0.9 \\ 0.5$	_	$\frac{6.0}{3.5}$	7.0 - 7.3 $6.8 - 7.1$	13.0 - 14.5 $13.0 - 14.5$	5.5-6.0 $5.5-6.0$	13.0 - 14.5 $13.0 - 14.5$	
05553+1631 $18089-1732$	1	197 31933	$^{-}$ 2448	$\frac{1.7}{17.0}$	180 1808	2.4 8.6	31.1	1.3	$^{2.4}$	$0.5 \\ 2.0$	>7.6 $8.0-8.5$	13.25 - 15.25 14.75	6.25 - 6.5 6.5 - 6.75	$13.25 - 14.75 \\ 14.75$	
18089-1732	2	5384	412	2.0	212	0.2	0.7	1.8	_	-	- 0.0	-	0.5-0.75	-	
	3 4	$\frac{2128}{5009}$	163 384	$0.9 \\ 2.3$	$\frac{93}{244}$	0.1	$0.5 \\ 3.0$	$0.6 \\ 1.5$	1.6	$0.5 \\ 1.0$	6.5 - 7.5	14.5 - 15.25	5.0 - 5.75	$^{-}$ 14.75	
$18090\!-\!1832$	$\frac{1}{2}$	4641 1523	2022	2.4	$\frac{255}{74}$	1.4	$\frac{2.1}{0.5}$	1.4	-	1.0	6.8 - 7.4	$14.5\!-\!15.0$	5.0 - 5.75	14.75	
$18102\!-\!1800$	1	23964	663 826	$0.7 \\ 2.9$	308	$0.3 \\ 0.3$	1.4	0.9	1.5	5.5	_	_	_	_	
18151 - 1208	$\frac{1}{2}$	1104 797	_	$\frac{4.4}{2.8}$	468 297	$\frac{4.6}{2.4}$	_	1.2	_	$0.5 \\ 3.0$	>7.5 7.5	14.25 - 14.75 $14 - 14.25$	$6.25 - 6.5 \\ 5.75$	14.75 $14.0 - 14.25$	
	3	270 64	-	1.0	103	0.7	-	0.8	-	0.5	6.9	13.25	5.25	13.25	
18159 - 1550	4 1	4873	786	$0.3 \\ 0.6$	35 63	$0.2 \\ 0.1$	0.2	0.9	1.4^{-}	9.0	6.4 - 7	14.5 - 15.0	5.0 - 5.75	14.75 - 15.0	
18182 - 1433	$\frac{1}{2}$	20719 1593	3013 231	$9.4 \\ 0.7$	999 76	$\frac{4.3}{0.1}$	$\frac{11.4}{0.3}$	1.8 0.9	2.5	$\frac{3.5}{4.5}$	7.5 - 8.4	14.75 - 15.5	6.0 - 6.75	15.25	
$18223\!-\!1243$	$\frac{1}{2}$	11841 2841	$\frac{1054}{253}$	2.0 0.8	212 79	0.3	$\frac{1.0}{0.4}$	1.2 1.6	_	$\frac{4.0}{7.5}$	7.0 - 8.0 $6.5 - 6.8$	14.5 - 15.0 $14.0 - 14.25$	5.5 - 6.25 5.00	$14.5 - 14.75 \\ 14.25$	
	3	3789	337	1.2	127	0.3	0.9	-	_	3.5	6.8 - 7.2	14.5 - 14.25 $14.5 - 14.75$	5.25	14.5 - 14.75	
18247 - 1147	4	1231 5318	$\frac{109}{2760}$	$0.3 \\ 5.1$	$\frac{34}{542}$	0.0 2.6	$\frac{0.2}{3.6}$	1.6	_	3.5	_	_	_	_	
	2	1371 1175	711 610	1.0 0.8	106 82	$0.2 \\ 0.2$	$0.3 \\ 0.2$	_	_	_	_	_	_	_	
	4	2603	1351	1.7	180	0.5	0.7	1.3	-	4.5	> 7.4	$15.0\!-\!15.75$	>6.5	15.50	
18264 - 1152 $18272 - 1217$	1	$55326 \\ 141$	4337	$\frac{16.0}{0.8}$	1702 87	5.6 0.9	19.9	$\frac{1.5}{0.9}$	2.2	$\frac{3.5}{1.5}$	7.5 - 9.0 $6.2 - 7.4$	14.25 - 15.0 14.75 - 15.5	6.25 - 7.0 5.25 - 5.75	14.75 15.00	
18290-0924	2	88 6466	$^{-}_{1647}$	$0.7 \\ 3.3$	$\frac{73}{351}$	0.8	$^{-}_{2.1}$	1.0	_	$^{-}_{6.5}$	6.2 - 7.6	$\begin{array}{c} - \\ 14.75 - 15.5 \end{array}$	5.25 - 6.0	15.00	
	2	8776	2236	3.5	372	1.2	2.5	-	_	_	-	-	0.20	-	
18306 - 0835	$\frac{1}{2}$	$\frac{16421}{2873}$	3443 602	$\frac{6.9}{2.0}$	$734 \\ 212$	$\frac{2.4}{1.0}$	$\frac{5.3}{2.1}$	1.5	1.5	3.5	_	_	_	_	
18308-0841	3	3848 12829	807 2690	1.0 4.6	104 489	$0.2 \\ 1.7$	$0.3 \\ 3.6$	1.7	_	6.5	_	_	_	_	
10000 0011	2	2873	602	1.7	180	0.3	0.7	-	_	-	-	-	-	_	
	3 4	$\frac{3489}{1077}$	$731 \\ 226$	$0.8 \\ 0.6$	88 65	$0.1 \\ 0.2$	$0.3 \\ 0.4$	_	_	_	_	_	_	_	
18310-0825	5 1	$872 \\ 15312$	182 3828	$0.5 \\ 1.8$	55 191	$0.1 \\ 0.2$	$0.2 \\ 0.5$	$^{-}_{1.4}$	1.5	6.0	>6.8	15.0 - 15.5	>5.75	15.25 - 15.5	
	2	5529 2381	1382 595	$\frac{2.5}{1.1}$	$\frac{265}{117}$	$0.7 \\ 0.3$	$\frac{1.4}{0.6}$	1.2	_	1.0	>7.5	15.25 - 15.75	>6.5	15.5 - 15.75	
	4	2126	531	1.0	105	0.2	0.5	_	_	_	-	_	_	_	
18337 - 0743	5 1	$\frac{1446}{22541}$	$\frac{361}{2727}$	$0.7 \\ 4.2$	$\frac{75}{446}$	$0.2 \\ 0.7$	$0.3 \\ 2.1$	1.3	$^{-}_{2.7}$	8.0	>7.0	14.75 - 15.5	>5.5	15.0 - 15.25	
	2	$\frac{4959}{1307}$	600 158	1.5 0.9	159 100	$0.3 \\ 0.4$	0.8 1.1	1.5	1.9	4.5	>7.0 >7.4	15.0 - 15.75 $12.5 - 15.5$	>6.0 >6.25	15.50 $12.5-15.25$	
18345 - 0641 $18348 - 0616$	1	6860 7298	3576	$^{2.4}$	255	0.7	_	1.5	3.5	6.0	-				
18348-0010	$\frac{1}{2}$	1905	933	$\frac{2.0}{1.0}$	$\frac{212}{106}$	$0.4 \\ 0.2$	$0.6 \\ 0.2$	1.2	_	10.0	_	_	_	_	
	3 4	$\frac{2067}{1581}$	$\frac{1013}{774}$	$\frac{1.0}{0.4}$	103 46	$0.2 \\ 0.1$	$0.3 \\ 0.1$	$0.5 \\ 0.8$	_	$0.5 \\ 8.5$	_	_	_	_	
	5 6	$1094 \\ 1378$	536 675	0.9 0.8	92 82	$0.3 \\ 0.2$	$0.4 \\ 0.3$	_	_	_	_	_	_	_	
40000 0544	7	1540	755	0.7	77	0.2	0.2	_	_	_	-	_	_	_	
18372 - 0541 $18385 - 0512$	1	$10198 \\ 13352$	$\frac{184}{311}$	$\frac{2.6}{4.5}$	$\frac{276}{478}$	$0.5 \\ 1.8$	$\frac{3.9}{11.6}$	$\frac{1.2}{1.6}$	1.2	$\frac{2.0}{2.0}$	_	_	_	_	
	2	3306 1716	$\frac{77}{40}$	$0.5 \\ 0.4$	$\frac{52}{44}$	$0.1 \\ 0.1$	$0.3 \\ 0.5$	1.9	_	9.0	_	=	_	_ _	
18426 - 0204 $18431 - 0312$	1	$\frac{10881}{3702}$	$\frac{72}{2471}$	$0.7 \\ 1.4$	$\frac{72}{148}$	$0.0 \\ 0.4$	$0.5 \\ 0.4$	0.6 1.8	$\frac{1.2}{1.9}$	$8.5 \\ 10.5$	_	_	_	_	
	2	2389	1595	1.3	138	0.4	0.5	-	-	_	-	_	_	_	
18437 - 0216	$\frac{1}{2}$	$\frac{2347}{693}$	_	$\frac{1.4}{0.6}$	148 63	$0.3 \\ 0.1$	_	0.9	1.3	7.0	_	_	_	_	
	3	933 800	_	1.0 0.8	102 80	$0.4 \\ 0.2$	_	1.5	_	6.5	_	_	_	_	
	5	720	-	0.7	77	0.2	-	_	_	_	-	_	_	_	
$18440\!-\!0148$	6 1	693 1717	_	$\frac{1.5}{0.4}$	$\frac{159}{37}$	$\frac{1.3}{0.1}$	_	2.1	_	8.0	_	_	_	_	
18445 - 0222	$\frac{1}{2}$	$\frac{4861}{857}$	$\frac{1545}{272}$	1.8 0.5	191 50	$0.4 \\ 0.1$	$0.7 \\ 0.2$	$\frac{1.2}{0.7}$	2.1	$\frac{3.5}{2.5}$	>6.8	14.75 - 15.25	5.5 - 6.25	15.00	
18447-0229	3	1315 2092	418 1355	0.8	87 92	0.2	0.4	1.7	$^{-}_{1.2}$	10.0	-	-	-		
	2	530	343	0.9	93	0.7	0.8	-	-	-	_	=	=	=	
18454 - 0136	$\frac{1}{2}$	$\frac{11965}{5221}$	$\frac{615}{268}$	$\frac{3.2}{1.7}$	340 180	$\frac{1.0}{0.6}$	$\frac{4.5}{2.6}$	_	_	_	_	_ _	_		
$18454\!-\!0158$	$\frac{1}{2}$	2774 2847	291 299	$\frac{1.5}{1.2}$	$\frac{159}{127}$	$\frac{1.1}{0.7}$	_	_	_	_	_	_	_		
	3	5111	537	1.9	202	1.1	-	-	-	_	-	_	_	-	
	4 5	$\frac{3066}{2044}$	322 215	$\frac{2.5}{0.9}$	$\frac{265}{90}$	$\frac{2.7}{0.5}$	_	_	_	_	_	_	_	_	
	6 7	803 1679	84 176	1.0 0.9	103 92	$\frac{1.0}{0.5}$	_	_	_	_	7.0	13.0 - 14.75	5.5 - 6.0	13.0 - 14.75	
$18460\!-\!0307$	1 2	3478	1042	1.2	127	0.3	0.5	1.1	2.1	7.0	>8.2	$13.0\!-\!15.25$	>6.25	13.0 - 15.0	
	3	$\frac{1428}{1135}$	$\frac{427}{340}$	0.7	73 54	0.1	0.3	_	_	_	_		_		
	4 5	$1025 \\ 1794$	307 537	$\frac{1.2}{0.3}$	$\frac{127}{34}$	$\frac{1.0}{0.0}$	$\frac{1.9}{0.1}$	_	_	_	=	_	_		
$\substack{18470-0044\\18472-0022}$	1	4192 11978	995	2.5 1.7	265 180	1.4	1.2	0.9	1.3	$^{-}_{3.5}$	>6.8 $7.0-8.0$	14.75 - 15.5 $12.75 - 15.0$	5.25 - 6.25 5.75 - 6.25	15.25 $12.75 - 15.0$	
101.2-0022	2	1331	110	0.5	53	0.1	0.3	-	-	-		-	-	-	
18488+0000	3 1	$\frac{1020}{6103}$	$\frac{84}{2246}$	$\frac{0.5}{2.9}$	$\frac{55}{308}$	$0.1 \\ 0.9$	$0.3 \\ 1.5$	1.3	2.5	$^{-}$	>8.0	13.25 - 15.0	>6.25	13.25 - 14.5	
18517+0437	2 1	$\frac{1109}{2310}$	408	1.2 6.8	$\frac{127}{723}$	$0.4 \\ 5.4$	0.7	$^{-}_{1.4}$	$^{-}_{1.7}$	$_{5.0}^{-}$	>7.4	$\begin{array}{c} - \\ 14.25 - 14.75 \end{array}$	>6.5	14.5 - 14.75	
18521+0134	2	160 2997	925	1.1	117 212	0.6 0.9	1.6	1.4	2.7	3.0	-		-		
18530 + 0215	1	12456	4280	3.6	382	0.8	1.3	1.1	1.8	2.0	>7.2	14.75 - 15.5	>6.0	15.0 - 15.5	
18540 + 0220 $18553 + 0414$	1	$\frac{2958}{15827}$	286 34	$0.6 \\ 3.6$	$\frac{60}{382}$	$0.1 \\ 1.2$	$0.3 \\ 26.3$	$\frac{1.1}{1.5}$	$\frac{3.0}{0.9}$	$\frac{10.0}{2.5}$	_	_	_	=	
18566 + 0408 $19012 + 0536$	1	2110 3885	1111	2.9 2.9	308 308	$\frac{1.8}{1.4}$	2.6	$\frac{1.7}{1.6}$	1.8 1.9	$9.0 \\ 3.5$	>7.0	$^{-}$ $14.75 - 15.5$	6.0 - 7.0	- 15.25	
19035 + 0641	1	386	_	1.9	202	1.8	_	1.4	1.7	7.0	> 7.25	14.25 - 14.5	5.75 - 6.25	$14.25\!-\!14.5$	
19074 + 0752 $19175 + 1357$	1	2160 2248	373 -	0.9 1.3	93 138	0.1 0.5	0.4	$\frac{0.9}{1.3}$	2.5	$\frac{2.5}{3.5}$	>7.2 > 7.2	$\substack{14.25-14.75\\14.25-14.75}$	5.75 - 7.0 $6.0 - 6.25$	$14.5 - 14.75 \\ 14.50$	
	2 3	$655 \\ 843$	_	$0.8 \\ 0.4$	81 46	$0.4 \\ 0.1$	_	_	_	_	_	_	_	_	
	4 5	$702 \\ 749$	_	$0.7 \\ 0.6$	73 59	$0.2 \\ 0.1$	_	0.7	_	$^{-}_{3.5}$	_	_	= =		

Figures 1-6: MAMBO 1.2 mm continuum maps. The axis show offsets in arcsec from the absolute IRAS-positions given in Sridharan et al. (2001). The greyscale and contours are chosen to highlight the most important features of each image, usually from 10% to 90% (step 10%) of the peak flux given in Table 2.

Figures 7-9: Example-fits of the radial profiles: an outer power law, and inner power law and an inner breakpoint where the power law stops and merges into a constant flux distribution.

Figure 10 (a) Histogram of inner radial index m_i ($I \propto r^{-m_i}$) for all sub-clumps, where fits were possible. (b) m_i histogram for different sub-groups: grey: strong in hot core tracer CH₃OH and/or CH₃CN and no resolved cm-emission; dotted line: resolved cm-sources; dashed line: CH₃OH and CH₃CN non-detections and no resolved cm-emission. (c) Histogram of the differences between m_o and m_i .

Figure 11: Results of the CS-LVG modeling: histograms of gas density distribution (a) and CS column density distribution (b).

Figure 12: (a) shows the linewidth correlation between $C^{34}S(2-1)$ and NH_3 . While filled and open circles represent $\Delta v(NH_3(1,1))$ and $\Delta v(NH_3(2,2))$, respectively, the asterisks and open triangles show $\Delta v(C^{34}(2-1))$ versus $\Delta v(NH_3(1,1))$ and $\Delta v(NH_3(2,2))$ data for a few UCHII regions (Churchwell et al. 1990; Cesaroni et al. 1991). In Figure (b) the $C^{34}S(2-1)$ linewidth are plotted versus the core mass (again from the dust continuum). Filled circles show sources from our sample, while asterisks and open squares represent data for UCHII regions (for details see the main text). The full line describes the expected relation in case of virial equilibrium. In both plots only sources without distance ambiguity (see Sridharan et al. (2001)) are included.

Figure 13: Linear breakpoint of the radial fits versus the corresponding core masses for sources without distance ambiguity. The straight line corresponds to breakpoint_{linear} $\sim M^{0.6}$. The sources shown as open circles were not included in the fit.

		Table 3—Continued													
	6	1780	_	0.5	54	0.1	_	0.4	_	1.5	_	_	_	_	
	7	936	_	0.4	37	0.1	_	-	_	-	_	_	_	_	
19217 + 1651	i	9518	_	5.3	563	2.0	_	1.6	2.0	3.5	>7.2	14.75 - 15.25	>6.0	15.0 - 15.25	
19220 + 1432	1	3406	_	1.8	191	0.7	_	1.4	1.8	9.5	7.0 - 7.5	14.25 - 14.5	5.5	14.25	
19266 + 1745	1	6263	5	3.3	351	1.1	36.7	1.6	2.0	5.0	6.8 - 7.2	14.25 - 14.75	5.25 - 5.75	14.50	
	2	1445	1	1.2	127	0.6	19.0	1.2	-	2.5	_	_	_	_	
19282 + 1814	1	2732	146	$^{2.4}$	255	0.9	3.9	0.9	2.1	2.5	7.2	13.25 - 13.5	5.50	13.25 - 13.5	
19403 + 2258	1	1582	229	0.5	50	0.1	0.1	0.6	1.2	2.5	> 7.0	14.25 - 14.5	5.5 - 6.0	14.25 - 14.5	
19410 + 2336	1	7761	835	5.7	606	$^{2.4}$	7.2	1.2	1.4	5.0	6.8 - 7.2	14.5 - 15.25	5.25 - 5.75	14.75	
	2	1724	185	1.6	170	0.5	1.4	0.7	_	2.5	7.6	13.25 - 13.75	6.00	13.25 - 13.75	
19411 + 2306	1	1960	490	1.7	180	0.8	1.6	1.5	_	8.5	>7	14.0 - 14.5	5.5 - 6.25	14.25 - 14.5	
	2	1447	361	0.7	78	0.2	0.3	0.5	-	5.0	_	_	_	_	
19413 + 2332	1	3288	230	1.1	117	0.4	1.4	1.0	1.2	6.5	7.2 - 7.6	14.5 - 15.0	5.5 - 5.75	14.75	
4048410044	2	1150	80	0.5	56	0.2	0.6	-	-	-		-	-	-	
19471 + 2641	1	110	-	1.4	148	2.4	-	0.7	1.3	0.5	7.6	13.25 - 13.75	6.00	13.25 - 13.5	
0005410405	2	52	-	0.5	55	0.6	-	-	-	-	. = -	-		-	
20051+3435	1	511 9	95	$\frac{1.0}{1.7}$	106 180	0.4 6.8	0.9	$\frac{1.0}{1.0}$	1.6	8.0 1.0	>7.2 $6.0-7.0$	14.5 - 15.0 $14.5 - 15.0$	>5.75 $4.75-5.5$	14.75 - 15.00 $14.75 - 15.5$	
20081 + 2720	2	1	_	0.6	61	4.6	_	1.0	_	1.0	6.0-7.0	14.5-15.0	4.75-5.5	14.75-15.5	
	3	1	_	0.6	46	3.0	_	_	_	_	_	_	_	_	
20126+4104	1	460	_	5.2	553	11.4	_	1.4	2.2	3.0	_	_	_	_	
20205+3948	1	548	_	0.7	70	0.2	_	1.1	2.0	8.5	_	_	_	_	
20203T3946	2	182	_	0.3	36	0.1	_	-	2.0	0.0	_	_	_	_	
20216+4107	1	171	_	1.8	191	3.1	_	1.3	1.6	6.0	>7.4	13.75 - 14.5	>6.0	14.0 - 14.5	
20293+3952	1	461	195	1.9	202	1.3	2.0	1.2	1.8	10.5	>7.2	14.25 - 14.75	>5.75	14.5 - 14.75	
20200 0002	2	77	32	0.6	58	0.4	0.6			-	Z		7 0.10		
20319 + 3958	1	87	~=	0.9	91	1.3	-	1.5	2.0	5.5	>7.5	14.5 - 15.0	>6.25	14.75 - 15.0	
20332 + 4124	1	1529	_	1.4	148	0.9	_	0.6	1.1	5.5	>7.0	14.5 - 15.0	5.5 - 6.0	14.75	
20343 + 4129	1	88	_	2.2	234	3.9	_	1.0	_	8.0	7.0 - 7.5	14.25 - 14.5	5.5 - 5.75	14.50	
	2	55	_	2.1	223	4.1	_	_	_	_	-	_	_	_	
	3	36	_	0.9	91	1.3	_	_	_	_	-	_	_	_	
22134 + 5834	1	436	-	1.1	117	0.7	_	1.3	1.9	8.0	> 7.4	14.75 - 15.25	>6.2	15.0 - 15.25	
22551+6221	1	33	_	0.7	73	1.5	_	0.5	1.0	9.0	7.0 - 7.3	12.75 - 14.25	5.5 - 6.0	12.75 - 14.0	
22570 + 5912	1	1469	_	1.2	127	0.5	_	1.1	1.6	6.0	>7.0	14.25 - 14.75	5.75 - 6.0	14.50	
	2	629	_	0.9	93	0.5	_	_	_	-	7.2 - 7.5	14.75 - 15.0	5.5 - 5.75	14.00	
	3	378	-	0.4	39	0.1	_	-	-	_	_	_	_	-	
	4	699	-	0.5	51	0.2	_	-	_	-	6.6 - 7.0	$14.0\!-\!14.25$	5.0 - 5.25	$14.0\!-\!14.25$	
23033+5951	1	2327	-	3.7	393	3.6	-	1.3	2.3	4.0	6.8 - 7.3	14.25 - 14.5	5.5 - 5.75	14.50	
23139+5939	1	1759	-	4.0	425	3.1	-	1.7	3.2	5.0	>7.2	14.5 - 15.0	>5.75	14.75-15.0	
23151+5912	1	1229	-	1.8	191	1.4	-	1.3	2.2	2.5	>7.4	14.5-15	6.25 - 6.75	14.75	
23545 + 6508	1 2	16 11	_	0.9	95 98	2.3 3.0	_	0.6	_	4.0	7.2 - 7.8	13.0-13.75	5.75 - 6.00	13.0-13.75	
	2	1.1	_	0.9	98	3.0	_	_	-	_	7.4 - 8.1	13.0 - 13.75	6.00	13.0 - 13.75	

 $\begin{array}{c} \text{Table 4} \\ \text{Parameters of the CS-fits} \end{array}$

	_	_		_	_	_	_														
$\frac{1}{05358+3543}$	2	-16.3	6.5	5 35.9	5.1	9.2	8 47.5	4.8	9.5	11 39	3.8	13	14	15	16	17	18	19	20	21	
05338+3543 05490+2658	1	0.7	2.2	3.9	1.6	2.8	5.1	1.7	1.6	3.3	1.8	_	_	_	_	_	_	_	_	_	
	2	0.3	3.3	8.9	2.5	3.4	9.8	2.7	2.3	6.1	2.4	-	-	_	-	-	-	-	-	-	
05553+1631	1	5.7	2.7	6.2	2.1	4	10.6	2.4	5.1	12	2.2	- 0.1	10.0				-	-	- 07	- 4.0	
18089-1732	1 4	$34.1 \\ 34.1$	$\frac{3.7}{2.1}$	$\frac{22}{10.1}$	$\frac{5.5}{4.5}$	6.5 3	$\frac{50.7}{15}$	$7.3 \\ 4.5$	13.6	97.3	6.7	$\frac{3.1}{0.4}$	$\frac{12.2}{1.2}$	$\frac{3.6}{2.6}$	$\frac{6.4}{0.6}$	$\frac{27.2}{1.4}$	$\frac{3.9}{2.2}$	8	37	4.3	
18090-1832	1	110.8	1.4	8.9	5.9	1.6	12.9	7.4	1.3	9.1	6.3	0.2	1.2	5.3	0.3	1.5	4	_	_	_	
18151-1208	1	33.4	8.8	26.6	2.8	12.9	39	2.8	14.4	45.4	2.9	1	2.9	2.5	_	_	-	-	_	-	
	2	29.7	4.1	18	4	5.4	29.2	5	3.6	13.3	3.4	0.3	1.6	4.5	-	-	-	-	-	-	
18159-1550	3 1	$30.7 \\ 60.3$	$\frac{2.7}{2.5}$	5.6 8.7	$\frac{1.9}{3.2}$	3.1 3.6	$\frac{4.7}{11.2}$	$\frac{1.4}{2.8}$	3.5	8.9	2.3	0.5	1.4	2.2	_	_	_	_	_	_	
18182-1433	1	59.1	6.9	30.4	4.1	9.3	47.4	4.7	11.3	49.9	4.1	2.1	8	3.5	2	9.3	4.2	5.1	22.4	4	
	2	40.6	1.3	4.3	2.9	1.5	4.4	2.7	-	-	_	-	_	_	-	-	_	-	_	-	
18223-1243	1	45.5	5.3	18.5	3.2	6.9	24.8	3.3	6.6	23	3.2	0.7	2.3	2.8	1.3	3.3	2.3	-	-	-	
	2	$\frac{44.9}{45.1}$	$\frac{2.3}{2.9}$	$\frac{8.5}{11.2}$	$\frac{3.4}{3.6}$	$\frac{2.3}{3.2}$	$\frac{8.1}{15.4}$	$\frac{3.2}{4.5}$	$\frac{0.9}{2.6}$	$\frac{3.7}{14.7}$	$\frac{3.5}{5.2}$	$0.2 \\ 0.4$	$^{1}_{1.7}$	$\frac{3.6}{3.2}$	_	_	_	_	_	_	
18247-1147	1	120.9	1.7	6.6	3.5	2.4	11.4	4.4	2.0		0.2	-		3.2		_	_	_		_	
	4	59.3	1.1	3.1	2.6	1.8	4.7	2.4	4.1	9.4	2.1	0.4	0.9	2.1	0.7	1.3	1.6	_	_	_	
18264-1152	1	43.6	8.9	42.6	4.4	12.3	66.4	5	14.5	81.4	5.2	1.1	3.7	3.1	1.9	7	3.4	-	-	-	
18272-1217	1	34.1	1.6	5.6	3.2	3.2	8.3	2.3	2.8	11.2	2.3	0.4	0.9	1.9	0.8	1.6	1.8	_	_	-	
18290-0924 18310-0825	1	84.3 84.0	$\frac{2.8}{2.5}$	$\frac{10.4}{9.5}$	$\frac{3.4}{3.5}$	$\frac{3.6}{3.1}$	$\frac{13.6}{12.2}$	$\frac{3.5}{3.6}$	$\frac{3.3}{4.4}$	$\frac{11.3}{12.9}$	$\frac{3.1}{2.7}$	$0.7 \\ 0.9$	$\frac{1.9}{2.2}$	$\frac{2.5}{2.2}$	1.2^{-1}	$\frac{2.4}{3.3}$	$\frac{2.1}{2.5}$	_	_	_	
10010 0020	2	83.5	1.3	10.4	7.2	2.1	17.6	7.7	6.8	41.2	5.6	0.6	2.4	3.5	1.2	5	3.6	_	_	_	
18337-0743	1	58.6	2.5	14	5.1	3.1	17.3	5.1	3.7	14.6	3.7	0.7	2.4	3.2	0.9	3.6	3.4	-	_	_	
	2	58.1	1.3	3.6	2.6	2.5	5.1	1.9	3.9	10.2	2.4	0.5	1.2	2.1	0.9	2.5	2.5	-	-	_	
18445-0222	3 1	55.5 86.8	$0.5 \\ 7.9$	$\frac{5.3}{26.7}$	$9.9 \\ 3.1$	$0.9 \\ 10.5$	$\frac{7.9}{37.4}$	$7.5 \\ 3.3$	$\frac{1.8}{11.4}$	$\frac{16}{41.9}$	8.1 3.4	1.8	- 5 e	2 0	3		2.6	_	-	_	
18445-0222 18454-0158	1	86.8 99.5	0.7	3.8	$\frac{3.1}{4.5}$	0.7	2.6	$\frac{3.3}{3.4}$	11.4	41.9	3.4	1.8	5.6	2.8	- -	8.8	2.0	_	_	_	
	2	97.5	1.1	9.6	7.7	0.9	7.1	7.1	_	_	-	_	_	_	_	_	_	_	-	_	
	3	96.5	1.6	12.5	6.9	1.7	13	6.9	-	-	-	-	-	-	-	-	-	-	-	-	
	4	101.1	1.8	7.7	4	2.3	7.1	2.9	-	-	-	-	-	-	-	-	_	-	-	_	
	5	94.5	1.2	6.2	4.8	0.9	5.5	$\frac{5.7}{2}$	1.0	2 =	1 7	-	_	_	-	_	_	-	_	_	
	6	$101.5 \\ 95.1$	$0.2 \\ 1.5$	$\frac{0.8}{5.7}$	$\frac{3.5}{3.4}$	$\frac{2.5}{1.2}$	$\frac{5.6}{4.9}$	3.7	1.9	3.5	1.7	_	_	_	_	_	_	_	_	_	
18460-0307	í	83.6	1.9	6.8	3.2	2.5	8.5	3.1	2.8	7	2.3	_	_	_	_	_	_	_	-	_	
18470-0044	1	96.5	5	23.5	4.3	7.4	34.2	4.2	7.2	29.1	3.7	1.6	5.2	2.9	2.9	8.9	2.8	_	_	_	
18472-0022	1	49.3	1.7	9.5	5	1.9	12.1	5.9	2.4	7.8	3	-	-	-	-	-	_	-	-	_	
18488+0000	1	82.6	2.4	18.8	7.1	4.3	32.4	7	5.9	36.2	5.7	1	- 2 0	- 2	1.0	6	-	_	_	_	
18517+0437 $18530+0215$	1 1	$\frac{43.9}{77.1}$	9.8 6.1	$\frac{38.9}{20.4}$	$\frac{3.7}{3.1}$	13.1 9	$\frac{56.2}{29.4}$	4	$\frac{16.3}{12.9}$	$69.8 \\ 40.6$	$^{4}_{2.9}$	1.4	$\frac{3.8}{3.9}$	$\frac{3.3}{2.6}$	1.8 2.9	6.8	$^{3}_{2.1}$	_	_	_	
19012+0536	1	65.5	3.5	16.2	4.2	5.2	27.8	4.9	8	46.6	5.4	1	3.8	3.5	2.3	7.9	3.6	_	_	_	
19035 + 0641	1	32.8	3.9	20.6	4.9	5.1	27.8	5	4.7	24.6	4.9	0.3	1.5	3.7	0.6	1.3	1.9	_	_	_	
19074 + 0752	1	55.4	3.4	11.9	3.2	4.6	15.3	3.1	6.6	19.3	2.7	0.4	1.3	2.6	0.6	1.6	$^{2.4}$	-	-	-	
19175 + 1357	1	14.4	1.8	6.4	3.3	3.6	12	3	4.1	14.3	3.2	0.1	0.8	3.9	0.5	1.9	3.4	-	-	_	
	4 6	$7.7 \\ 7.6$	$0.7 \\ 1.5$	$\frac{3.3}{4.8}$	$^{4}_{2.9}$	$0.7 \\ 1.5$	$\frac{2.1}{3.5}$	$\frac{2.6}{2.1}$	$0.3 \\ 0.6$	3.8 1.1	9.9 1.8	_	_	_	_	_	_	_	_	_	
19217 + 1651	1	3.6	3.5	23.2	6.1	4.9	33.6	6.4	7	38	5.1	0.8	3.2	3.5	1.1	4.8	3.9	_	_	_	
19220 + 1432	1	69.1	2.7	11.8	3.9	3.6	16	4.1	2.3	8.4	3.3	0.3	1.1	3.4	_	_	-	-	_	-	
19266 + 1745	1	5.1	3.9	17.2	4.1	5.9	27.9	4.4	6	29.7	4.6	0.5	2.2	3.7	0.8	3.3	3.5	-	_	_	
19282+1814	1	23.0	3.6	7.5	1.9	3.8	8.2	2	2.1	4.6	2			1.5	-	1		_	_	-	
19403+2258 $19410+2336$	1	$\frac{26.5}{22.5}$	$\frac{4.2}{8.2}$	$\frac{6.4}{27.2}$	$\frac{1.4}{3}$	$\frac{5.5}{9.4}$	$\frac{7.1}{31.3}$	$\frac{1.2}{3.1}$	$\frac{5.4}{9.5}$	$\frac{6.3}{26.9}$	$^{1}_{2.6}$	$0.4 \\ 1.7$	$0.7 \\ 4.4$	$\frac{1.5}{2.4}$	$0.6 \\ 2$	4.8	$\frac{1.4}{2.1}$	_	_	_	
13410 2330	2	21.6	4.5	16.7	3.4	4.7	17.4	3.4	3.9	13.4	3.1	-		2.4	_	-	2.1	_	_	_	
19411 + 2306	1	29.3	3.7	11	2.7	5	13.4	2.5	5.3	12.3	2.1	0.2	1.1	3.7	0.6	1.7	2.3	_	_	_	
19413 + 2332	1	20.4	3.8	11.1	2.7	3.5	10	2.6	3.2	8.6	2.5	0.6	2.2	3.1	-	-	-	-	-	-	
19471+2641	1	23.3	4	10.8	2.5	5.2	13.9	2.5	4.3	10.6	2.2	-	_	-	_	-		-	-	_	
20051+3435 $20081+2720$	1	$\frac{11.9}{5.4}$	$\frac{2.4}{3.9}$	8 7.1	3 1.6	$\frac{3.3}{4.8}$	$\frac{7.8}{8.2}$	$\frac{2.2}{1.5}$	$\frac{3.2}{3.4}$	$9.3 \\ 5.4$	$\frac{2.6}{1.4}$	$0.4 \\ 0.8$	$^{1}_{1.2}$	$\frac{2.2}{1.3}$	$0.7 \\ 0.9$	1.3 1.3	$\frac{1.7}{1.3}$	_	_	_	
20205+3948	1	-1.9	1.9	2.8	1.3	2.6	4.4	1.5		- 0.4		-		-	-	-	-	_	_	_	
20216 + 4107	1	-1.6	3.9	8.3	1.9	5.3	10.4	1.8	6.4	19	2.7	0.2	0.6	2.6	-	-	_	_	-	_	
20293 + 3952	1	6.2	7.9	23.1	2.7	11.8	34.9	2.7	11	29	2.4	0.9	2.2	2.3	1.6	4	2.2	-	_	_	
90910 9050	2	6.1	2.7	9.5	3.2	1.9	6.6	3.2	7 2	15 4	1.0			1.0	_	_	_	_	_	_	
20319+3958 $20332+4124$	1 1	8.3 -2.8	$\frac{2.2}{2.9}$	$\frac{4.6}{10.4}$	1.9 3.3	$\frac{4.7}{3.9}$	$9.7 \\ 13.1$	$\frac{1.9}{3.1}$	$\frac{7.3}{4.2}$	$\frac{15.4}{12.9}$	1.9 2.8	$0.3 \\ 0.5$	$0.6 \\ 1.5$	$\frac{1.9}{2.5}$	0.6	1.6	2.3	_	_	_	
20343+4129	1	11.4	6.2	17.8	2.6	7.3	21.3	2.7	5.1	12.3	2.2	0.8	1.9	2.2	1	2.2	2.3	_	-	_	
22134 + 5834	1	-18.1	3.3	11.3	3.1	5	15.8	2.9	7.2	16.7	2.1	0.7	1.3	1.7	1.2	2.3	1.7	_	_	_	
22551+6221	1	-13.4	1.1	2.4	1.9	1.5	2.8	1.7	0.8	1.2	1.3	-	_		_		_	-	-	-	
22570 + 5912	1 2	-45.7 -48.0	$\frac{3.2}{3.9}$	$7.1 \\ 11$	$\frac{2.1}{2.6}$	5 4.9	$11.1 \\ 14.8$	2.8	$\frac{5.7}{4.3}$	12.3 13.3	2.8	$0.4 \\ 0.3$	$0.7 \\ 0.7$	1.7	$0.7 \\ 0.2$	1.5	3.3	_	-	_	
	4	-48.0 -46.6	3.6	9.5	$\frac{2.6}{2.4}$	4.9	10.4	2.8	1.6	3.3	1.8	0.3	0.7	1.9	$0.2 \\ 0.4$	0.7^{1}	1.7	_	_	_	
23033+5951	1	-53.0	7.3	28	3.5	9.5	35.5	3.4	7.4	27.8	3.5	1	2.7	2.4	1.2	3.9	3	_	-	_	
23139 + 5939	1	-44.6	5.2	24.5	4.4	7	38	5	8	39.3	4.5	0.8	2.5	2.8	1.3	4.1	2.9	-	-	-	
23151+5912	1	-54.4	3.8	10.9	2.6	6.4	20.1	2.9	9.2	37.1	3.7	0.5	1.4	2.7	1	3.2	2.8	-	-	_	
23545 + 6508	1	-18.4	1.9 1.9	3.3	1.6	2.8	4.4	1.4	1.5	2.1	1.3	_	-	_	_	_	_	_	_	_	
18247-1147	1	-18.0 56.2	0.3	3.7 0.7	1.8	3.3	5.6	1.5	2.8	4.3	1.4										
18247-1147	1	120.7	1.8	6.7	3.5	$^{-}_{2.4}$	11.4	4.5	_	_	_	_	_	_	_	-	_	_	_	_	
18247-1147	4	59.4	1.1	3.1	2.6	1.8	4.8	2.5	4.1	9.5	2.2	0.4	1.0	2.1	0.8	1.3	1.7	-	-	-	
18454-0158	1	52.6	0.8	1.9	2.3	-	_	_	-	-	-	-	-	-	-	-	-	-	-	-	
18454-0158	1	99.5	0.8	3.8	4.6	0.7	2.6	3.4	-	-	-	-	-	-	-	-	-	-	-	-	
18454-0158 18454-0158	2 2	$51.8 \\ 97.6$	$\frac{0.8}{1.2}$	3.1 9.6	$\frac{3.7}{7.8}$	$0.8 \\ 0.9$	$\frac{2.7}{7.1}$	$\frac{3.3}{7.2}$	_	_	_	_	_	_	_	_	_	_	_	_	
18454-0158	3	96.5	1.7	12.6	6.7	1.8	13.0	7.0	_	_	_	_	_	_	_	_	_	_	_	_	
18454-0158	4	101.1	1.8	7.8	4.1	2.3	7.2	3.0	_	_	-	_	_	_	_	_	_	_	-	_	
18454-0158	5	51.0	0.4	1.2	2.8	_	-	-	-	_	-	_	-	_	_	-	_	_	_	_	
18454-0158	5	94.6	1.2	6.2	4.9	0.9	5.6	5.7	-	_	-	-	-	-	-	-	_	-	-	_	
18454-0158	6 6	51.5	1.9	5.2	2.5	2.6	5.6	2.1	1.9	3.6	1.8	_	_	_	_	_	_	_	-	_	
18454-0158 18454-0158	7	101.5 95.1	$0.2 \\ 1.6$	$0.9 \\ 5.8$	$\frac{3.5}{3.4}$	1.2	5.0	3.8	_	_	_	_	_	_	_	_	_	_	_	_	
19175+1357	1	6.7	0.9	2.1	2.3		-	-	_	_	_	_	_	_	_	_	_	_	_	_	
19175 + 1357	1	14.5	1.8	6.5	3.4	3.8	12.0	3.1	4.1	14.3	3.3	0.5	2.0	3.5	-	-	-	-	-	-	
19175+1357	4	7.7	0.8	3.4	4.0	0.8	2.2	2.6	0.4	3.8	10.0	-	-	_	-	-	_	-	_	_	
19175+1357	6	7.6	1.6	4.9	3.0	1.6	3.6	2.1	0.6	1.2	1.8	_	_	_	_	_		_	_	_	

Note. — The first three columns show the source name, the peak number and the v_{LSR} (as taken from the CS 2–1 fit), the following 18 columns present the peak temperatures T_{mb} , the integrated intensities $\int T_{mb} dv$ and the line widths Δv of CS 2–1 (columns 4-6), CS 3–2 (columns 7-9), CS 5–4 (columns 10-12), C³⁴S 2–1 (columns 13-15), C³⁴S 3–2 (columns 16-18), and C³⁴S 5–4 (columns 19-21), respectively.

This figure "f1.jpg" is available in "jpg" format from:

This figure "f2.jpg" is available in "jpg" format from:

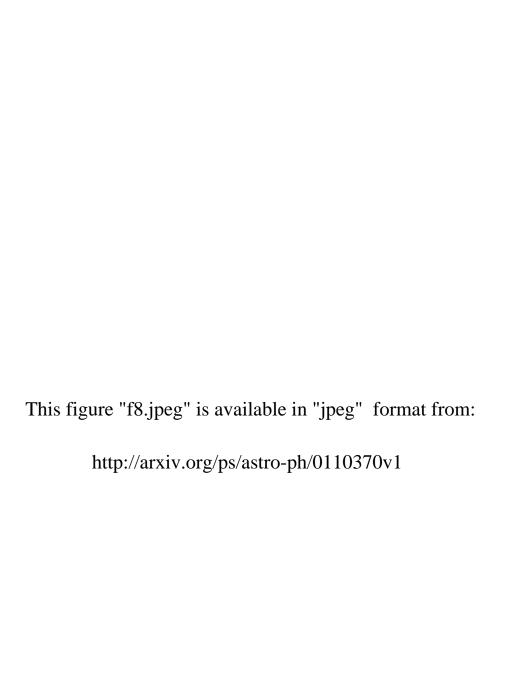
This figure "f3.jpg" is available in "jpg" format from:

This figure "f4.jpg" is available in "jpg" format from:

This figure "f5.jpg" is available in "jpg" format from:

This figure "f6.jpg" is available in "jpg" format from:

This figure "f7.jpeg" is available in "jpeg" format from:



This figure "f9.jpeg" is available in "jpeg" format from:

This figure "f10.jpeg" is available in "jpeg" format from: http://arxiv.org/ps/astro-ph/0110370v1

This figure "f11.jpeg" is available in "jpeg" format from:

This figure "f12.jpeg" is available in "jpeg" format from:

This figure "f13.jpeg" is available in "jpeg" format from: